Deciphering Radiolytic Oxidation in Halide Aqueous Solutions: A Pathway Toward Improved Synchrotron NAP-XPS Analysis

Héloïse Tissot, Romain Coustel, François Rochet, Anthony Boucly, Cédric Carteret, Erwan André, Fabrice Bournel, Jean-Jacques Gallet

▶ To cite this version:

Héloïse Tissot, Romain Coustel, François Rochet, Anthony Boucly, Cédric Carteret, et al.. Deciphering Radiolytic Oxidation in Halide Aqueous Solutions: A Pathway Toward Improved Synchrotron NAP-XPS Analysis. Journal of Physical Chemistry C, 2023, 127 (32), pp.15825-15838. 10.1021/acs.jpcc.3c03676 . hal-04285240

HAL Id: hal-04285240
https://hal.science/hal-04285240

Submitted on 19 Jan 2024

Deciphering Radiolytic Oxidation in Halide Aqueous Solutions: A Pathway Towards Improved Synchrotron NAP-XPS Analysis

Héloïse Tissot[1]*, *Romain Coustel*[2]*, *François Rochet*[3]*, *Anthony Boucly*[3†], *Cédric Carteret*[2], *Erwan André*[2], *Fabrice Bournel*[3,4] *and Jean-Jacques Gallet*[3,4]

[1] Université de Lille, CNRS, Unité de catalyse et de Chimie du Solide, UMR 8181, 59655 Villeneuve d'Ascq, France

[2] Université de Lorraine, CNRS, UMR 7564, Laboratoire de Chimie Physique et Microbiologie pour les Matériaux et l'Environnement, 54000 Nancy, France

[3] Sorbonne Université, CNRS, Laboratoire de Chimie Physique matière et Rayonnement, UMR 7614, 4 place Jussieu, 75005 Paris, France

[4] Synchrotron SOLEIL, L'Orme des Merisiers, Saint-Aubin - BP 4891192 Gif-sur-Yvette CEDEX, France

KEYWORDS. Water, halides, soft X-rays, synchrotron radiation, near ambient pressure, X-ray photoelectron spectroscopy, radiolysis.

ABSTRACT Synchrotron radiation near ambient pressure X-ray photoemission spectroscopy (SR NAP-XPS) has been an invaluable tool for examining gas/liquid and liquid/solid interfaces. Despite its benefits, concerns have emerged regarding beam damage in NAP-XPS experiments, particularly involving condensed liquid water, because of the high dose rates, greater than 10^5 Gy·s^{-1}. This study investigates the radiolytic effects on the chemistry of concentrated NaX sodium halide solutions (X = Cl, Br, I) and Mg-Cl solution formed over the layered double hydroxide $[Mg_2Al(OH)_6]^+[Cl^-]$. The formation of the oxidized species XO^- as the radiolytic end product under soft X-ray irradiation is discussed in detail. We examine the impact of known parameters (such as dose rate) on the abundance of XO^-. The observed scatter in the data likely arises from still unrecognized or insufficiently controlled parameters (such as solute concentration or solution hydrodynamics). Deciphering these radiolytic effects in halide solutions allows us to propose guidelines for their better identification, understanding and control, ultimately improving the reliability of synchrotron NAP-XPS analysis for interfaces relevant to environmental chemistry and electrochemistry.

INTRODUCTION

Since its inception in the early years of the 21st century,[1] Near Ambient Pressure XPS (NAP-XPS) has emerged as a versatile and powerful technique for examining solid or liquid surfaces in the presence of a gas phase, offering insights into their electronic structure and chemistry at atomic and molecular levels. While NAP-XPS has proven invaluable for studying gas/liquid[2] and gas/solid[3,4] interfaces (including electrochemical interfaces[5,6]), the high flux of soft X-rays produced by Synchrotron Radiation (SR) may cause beam damage during NAP-XPS experiments, particularly when involving condensed liquid water. Recognition and consideration of these effects, however, are relatively recent developments. For instance, in 2018, Boucly et al.[7] reported that pyridine intercalated between the layers of a hydrated swelling smectite mineralized to N_2. In this case, both water confinement effects and electron-hole pair formation in the wide band gap of aluminosilicate oxide layers likely enhanced water radiolysis.[8,9] Similarly, Weatherup and colleagues warned about the generation of radical species due to radiolysis during atmospheric pressure soft X-ray absorption studies of aqueous solutions in electrochemical cells in their 2017 publication.[10]

Due to their relevance in environmental chemistry, the surface chemistry of alkali halide solutions has been intensively studied by SR NAP-XPS. In particular, the pioneering NAP-XPS study (2012) by Cheng et al.[11] examined the deliquescence of alkali halides. In the case of NaCl, they observed a Cl 2p doublet chemically shifted to a higher binding energy (HBE) compared to the X^- halide doublet. They attributed the HBE doublet to surface X^- ions experiencing a different solvation environment at the gas/water interface than in the bulk. Our NAP-XPS study of 2015,[12] which probed the in-depth distribution of Na^+ cations in concentrated NaCl, NaBr and NaI solutions, also identified an HBE component alongside the expected X^-, aligning with observations of Cheng and coworkers. Although we contemplated the possibility of halide species in an oxidation state greater than −1, our primary interpretation of the HBE component concurred with the view of Cheng et al. of it as a surface species. In contrast, liquid jet XPS (LJ-XPS) studies of alkali halide solutions revealed X^- ions in a single chemical environment, as illustrated by the study of Cl^- in KCl solutions carried out by Eriksson et al..[13] This inconsistency could have been attributed to radiolysis effects affecting SR NAP-XPS (despite the strategy of collecting each set of spectra at a new sample spot[11]) while LJ-XPS is relatively immune to SR-induced beam damage because the liquid sample is constantly refreshed. Nevertheless, concerns about potential SR damage during NAP-XPS measurements lingered, as the samples studied in LJ and NAP-XPS were not entirely identical. First, LJ-XPS is restricted to dilute solution (~10^{-3} mol×L^{-1}), as the nozzle can be clogged by salt crystals at high concentrations, while highly concentrated solution droplets can be formed in the NAP-XPS setup. Second, water surfaces in NAP-XPS chambers are consistently covered by organic contaminants,[14] in contrast to the pristine surfaces of LJ-XPS due to continuous liquid renewal. The presence of contaminants at the gas/liquid interface could account for the varying chemical environments of halide anions.[12,14] Third, water jets in LJ-XPS are most of the time generated under non-equilibrium conditions. As evaporation takes place within the analysis chamber, this could potentially impact the gas/liquid interface (more recent experiments using jets in equilibrium with the vapor have demonstrated that this concern is ultimately irrelevant[15]).

Despite initial reluctance to recognize the radiolytic effects occurring during NAP-XPS experiments and dramatically highlighted in the article by Boucly et al.,[7] it has now become crucial to accept their existence. Therefore, previous interpretations of NAP-XPS halide core-level spectra[11,12,16] need a reassessment. This is further driven by the recent (2023) NAP-XPS study by Coustel et al.[17] on hydrated chloride-containing layered double hydroxide $[Mg_2Al(OH)_6]^+[Cl^-, yH_2O]$, which indicated that radiolytic effects influenced the chemistry of the halide.

The mechanisms of radiolysis in water are highly intricate, involving a multitude of intermediate species, ions, and radicals whose composition changes over time and is influenced by factors such as particle trajectory, energy, radiation dose, solute concentration, and pH. In solutions that are dilute, with concentrations of 10^{-3} M or lower, the direct ionization of the solute is negligible, as the majority of the radiation energy is absorbed by the solvent. The primary particles' energy deposition leads to the ionization ($H_2O^{\bullet+}$) and excitation (H_2O^*) of water molecules (occurring on a femtosecond timescale), along with the production of sub-excited electrons. Subsequently, water molecules undergo dissociation processes and ion-molecule reactions (taking place on a femtosecond to picosecond timescale) that generate various radicals, molecular products, and thermally equilibrated, solvated electrons (e_{aq}^-). In the final stage (taking place on a picosecond to microsecond timescale), the species react within the particle tracks and then diffuse throughout the solution.[18] The following radiolysis products of water have been detected either directly or indirectly (through the use of scavengers[19]): $HO^\bullet$, $H^\bullet$, e_{aq}^-, $H_3O^{\bullet+}$, $HO_2^\bullet$,H_2O_2, H_2.

However, the radiolysis of halide aqueous solutions presents specific features with respect to the case of pure water. In that respect, pulse radiolysis studies have provided a plethora of information.[20,21,22] Naturally, $H_2O^{\bullet+}$ can react with another water molecule to produce $HO^\bullet$ and H_3O^+ as in pure water, but its reaction with X^- to give $X^\bullet$ become increasingly significant as the solute concentration increases, as well as the direct ionization of X^- to $X^\bullet$.[21] This results in the formation of $X_2^{\bullet-}$, which can subsequently evolve into stable compounds such as X_3^-. For instance, this occurs for Br^- on a millisecond timescale[21] and is likely the case for I^-, given that I_3^- and Br_3^- have the highest stability constant in the X_3^- series.[23] These species' presence is confirmed by steady-state radiolytic studies involving doses in the range of 100 kGy.[24,25] A scheme of the reaction paths inspired by ref [21] (blue lines) is given in Figure 1.

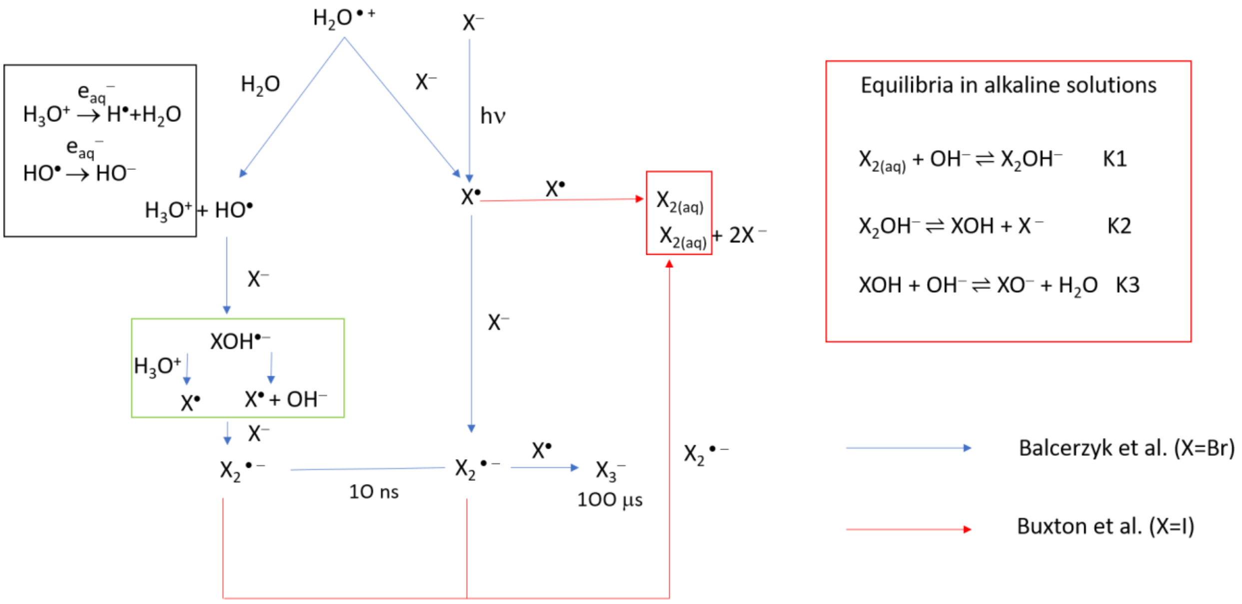

Figure 1. Scheme of X^- oxidation mechanisms in concentrated aqueous solutions, according to Balcerzyk et al.[21] at neutral pH (X=Br, blue lines) and Buxton et al.[26] at alkaline pH (X=I, red lines and frame). Recombination with the solvated electron e_{aq}^- leading to the neutralization of H_3O^+ are indicated within the black frame. X^- is oxidized indirectly through the reactions with radicals $HO^\bullet$ from water decomposition and directly by ionizing particles (hν, *e*). Green frame: reactions leading to pH increase). X_3^- is not observed in the present study. The observed products XO^- are those expected at alkaline pH.

While the latter studies are made at neutral pH, at alkaline pH the radiolysis of I^- solutions leads to the formation of $I_{2(aq)}$ (red lines in Figure 1), whose ultimate hydrolysis species are I_2OH^-, IOH and IO^-.[26,27] Regarding the radiolysis products of chloride, short timescale (picosecond to nanosecond) products are identified as $Cl_2^{\bullet-}$ and $ClOH^{\bullet-}$.[22] They can subsequently undergo a cascade of further reactions. *Steady-state* studies, such as the work of

Kelm et al.,[28] revealed that nearly saturated solutions of NaCl exposed to high doses of 10^6 Gy (at a pH of 12) result in the formation of hypochlorite ClO^-.

The current study examines the radiolytic effects induced by soft X-ray SR irradiation in halide aqueous solutions. SR with NAP-XPS serves as both the source and probe of radiolytic chemistry. We reassess and reinterpret a large body of NAP-XPS data (partly published in ref.[12]) regarding the chemical evolution of concentrated NaX sodium halide solutions (where X = Cl, Br, and I), and investigate new data regarding the Mg-Cl solution[17] formed over the layered double hydroxide (LDH) $[Mg_2Al(OH)_6]^+[Cl^-, yH_2O]$. Due to the limited penetration of the soft X-rays in water (0.7-5 μm in the 200 to 1200 eV range), surface dose rates higher than 10^5 $Gy \cdot s^{-1}$ are achieved. In the NAP-XPS chamber, the irradiated solution constitutes an open system, as it comprises water droplets in equilibrium with gas-phase water, allowing for gas exchanges between the liquid and gas phases.

We also provide a comprehensive analysis of halide radiolytic species formation and steady-state concentration as a function of photon energy, flux and dose rate. For halide X^- solutions, the XPS core-level binding energies indicate the formation of the oxidized XO^- species. As this conclusion is unexpected for I^- and Br^-, considering prior pulse and steady-state radiolytic studies,[20,21,24,25] we consider an alternative explanation – namely, the reaction of $X^\bullet$ radicals with surface-adsorbed organic contaminants – but we do not find any substantial confirmation for it. Consequently, we discuss the conditions (such as pH) leading to the observation of hypohalites. Regarding the hypochlorite species, the most convincing evidence of its generation under the SR beam was obtained by monitoring its disproportionation reaction during the drying of the LDH solution in the NAP-XPS analysis chamber. Finally, we offer guidelines for better understanding, controlling, and exploiting radiolytic effects in the context of SR NAP-XPS experiments.

METHODS

The experiments were conducted at TEMPO beamline (SOLEIL synchrotron facility), utilizing the near ambient pressure XPS (NAP-XPS) end station. The analysis/reaction chamber can operate up to 20 mbar and houses a PHOIBOS 150-NAP electron analyzer, manufactured by SPECS (Berlin). To maximize photoelectron signal intensity, an electrostatic lens system focuses the photoelectrons, and the analyzer aperture (with a diameter of 0.3 mm), is positioned approximately 1 mm from the sample surface (the nozzle is shown in Figure 2(a)). The acceptance angle is ±22°. The beamline and the analyzer are shielded from high pressures in the NAP chamber by differential pumping.[29] The sample holder is mounted on a vertical manipulator, with the analyzer axis perpendicular to the sample surface. The windowless beam entrance axis forms a 54.7° angle with the analyzer axis, resulting in an incidence angle (θ) of 35.3° between the beam and the sample surface. With a horizontal polarization, the angle between the radiation electric field and the axis of the analyzer lens is 35.3°.

High-purity NaCl, NaBr, and NaI salts (>99.9-99.999%) were purchased from Sigma-Aldrich. The chloride-containing layered double hydroxide (LDH) material $[Mg_2Al(OH)_6]^+[Cl^-, yH_2O]$ (referred to as MgAl-Cl-LDH) was produced as described in ref [17]. The powders were deposited on a gold substrate. Water pressure was introduced into the analysis chamber from a vial containing ultrapure water (>18 MΩ×cm), which was carefully degassed after several pump-thaw cycles (de-aerated water). By lowering the sample temperature using a circulating chiller and a Peltier block attached to the sample holder, water condensation on the powders was achieved, as shown in Figure 2(a). Close-to-saturation NaCl, NaBr, and NaI solutions were examined by NAP-XPS measurements at 5°C (278 K) and under a water vapor pressure P_w of 8 mbar. Droplets of typical diameter ~1 mm form on the substrate. They may also grow bigger, and reach diameters of 2-3 mm, see Figure 2(a). Probably due to the depression[30] created at the nozzle pin-hole by the differential pumping of the entrance lens, the surface of the droplets is animated by streams that are highlighted by the movement of solid salt particles with velocities on the order of 1 mm s^{-1}. It is also clear that the stream velocity depends on the sample-pinhole distance. Consequently, there is a certain level of solution renewal as the liquid remains in motion. However, these velocities are significantly lower compared to the velocities of liquid jets typically used in photoemission experiments (for a 40-μm diameter jet and a typical flow rate of 2.5 $mL\cdot min^{-1}$,[31] a velocity of 33 $m\cdot s^{-1}$ can be achieved).

A water layer was also formed above the MgAl-Cl LDH powder at a temperature of 1°C (274 K) and under P_w=4.5 mbar.

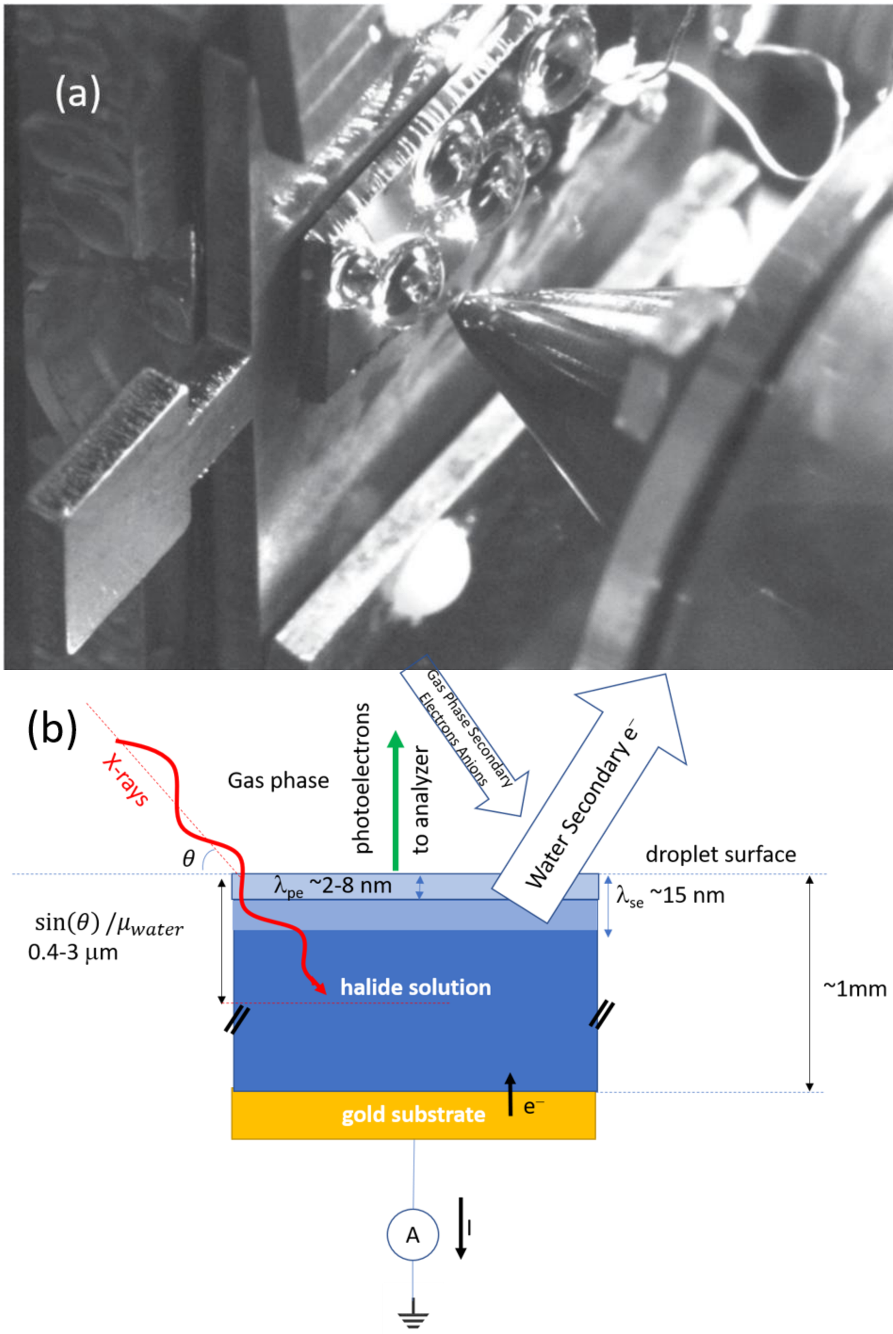

Figure 2. (a) Water droplets condensed on the gold surface in the analysis chamber during XPS acquisition. (b) Schematic representation of the liquid sample measurement. The beam incidence angle θ is 35.3°. Characteristic attenuation lengths of photons ($d_{ir} = \sin(\theta)\,/\mu_{water}$) and secondary electrons (λ_{se}), as well as the inelastic mean free path of photoelectrons (λ_{pe}) are

provided (note that μ_{water} depend on hν and λ_{pe} on the photoelectron kinetic energy, i.e. on hν). A sample current was measured only for the NaI solution (run#1, see below).

Photon flux. For the NAP-XPS branch of TEMPO beamline, photon flux (Φ) variations can be estimated from the I_0^{wire} current of a stainless-steel filament positioned on the beam path in the differentially pumped beam-entrance. The method is given in section S1 of the supporting information. We present in Table 1 the ratio $\Phi/_{\Phi_{max}}$, where Φ_{max} is the photon flux at $h\nu$ = 200 eV. In UHV conditions, ~10^{13} photons × s^{-1} reach the sample at this energy. With an X-ray spot area of 8×10^{-3} mm^2, the photon flux is around 1.3×10^{17} photons·cm^{-2} s^{-1} at 200 eV. Along its path across the gas phase (about 5 cm), the photon flux loss due to absorption is almost negligible under the current pressure conditions (<10 mbar).[7]

$h\nu$ (eV)	Φ/Φ_{max}	μ_{water} (μm^{-1})	$\dot{D}_w$ 10^5 Gy·s^{-1}
200	1.0	1.271	541
360	$1.7\ 10^{-2}$	0.280	3.7
400	$6.0\ 10^{-2}$	0.215	10.8
500	$9.6\ 10^{-2}$	0.122	12.5
600	$2.3\ 10^{-1}$	1.490	424
800	$8\ 10^{-3}$	0.729	10.0
1000	$3.5\ 10^{-3}$	0.412	2.9
1060	$3.7\ 10^{-3}$	0.353	2.9
1200	$2.0\ 10^{-3}$	0.253	1.3

Table 1. Normalized photon flux Φ/Φ_{max}(Φ_{max}=1.3 × 10^{17} photons × cm^{-2} × s^{-1}), the linear absorption coefficient of pure water $\mu_{water}$and the dose rate $\dot{D}_w$ (Gy·s^{-1}) calculated for pure water. The sample current measured in the case of the NaI solution.

Presumably, the surface radiation dose rate $\dot{D}_w$ plays a crucial role in understanding the equilibrium concentrations of radiolytic species. $\dot{D}_w$ (in Gy·s^{-1}) is calculated considering the fact that energy is deposited over a characteristic distance of $1/\mu_{water}$:

$$\dot{D}_w = \Phi \times h\nu \times \mu_{water} \times \rho^{-1} \qquad (1)$$

where μ_{water} (retrieved from the website CXRO X-Ray Interactions With Matter[32]) is the linear absorption coefficient of pure water and ρ is the density of water. The calculation of the dose rate does not consider the oxidation of X^{-} to $X^{\bullet}$.

When solution droplets are analyzed, the absorbed dose cannot be simply calculated by multiplying $\dot{D}_w$ by the measurement time of an XPS experiment (typically one minute per scan) due to the liquid movement mentioned earlier. Considering an X-ray beam with a diameter of 0.1 mm and a stream velocity of 1 mm.s^{-1}, the irradiation time is ~0.1 s. As a result, doses exceeding 10^4 Gy are applied.

Sample current measurement

Upon X-ray irradiation secondary electrons originating from inelastically scattered photoelectrons and Auger electrons leave the surface of the droplets (Figure 2(b)). Their effective escape depth λ_{se} in water is not known precisely. However, typical λ_{se} of~15 nm in solid insulators (oxides) are reported in the literature.[33] Given that inelastic mean free paths in liquid water[34] are slightly larger but close to those of the so-called universal curve for solids, the latter λ_{se} value of ~15 nm will be retained. This value is about one order of magnitude smaller than the photon penetration depth $d_{ir} = \sin(\theta)/\mu_{water}$ (θ=35.3° is the angle between the beam direction and the sample surface) that is in the 0.4–3 µm range in pure water. Note that the XPS probed depth is smaller than λ_{se}, as the escape-depth of photoelectrons λ_{pe} in pure water is in the range 2 nm (at a kinetic energy of 150 eV) – 8 nm (at a kinetic energy of 1100 eV).[12]

Due to secondary electrons escaping from the water surface, the solution surface should charge positively. As the metallic substrate is grounded, electrons can be provided by the ground to the solution (see Figure 2(b)). In addition, negative species (electrons, anions) from the gas phase can also land on the water surface to compensate the charge.[7] In the case of the NaI solution, we have measured a non-negligible "sample current", with an intensity in the 0.7-2.6 nA range. We report the current intensity in Figure 3 as a function of hν. $\dot{D}_w$ (from Table 1) is also plotted. It appears that the current roughly scales with the logarithm of $\dot{D}_w$. This suggests a saturation effect of the secondary electron current with the dose rate. Nevertheless, the dose rate and current maxima coincide at hν=200 eV and 600 eV (above the O K edge).

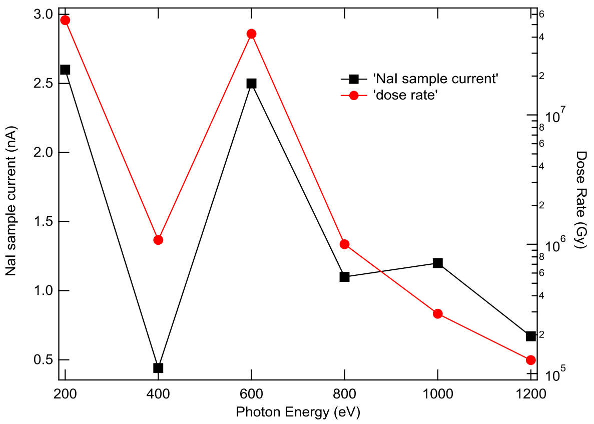

Figure 3. NaI solution “sample” current and dose rate $\dot{D}_w$ (logarithmic scale) as a function of hν. Electrons are provided to the solution.

Importantly, the sign of the current indicates that electrons are provided from the ground to the solution (this means the secondary electron current is greater in modulus than that of the negatively charged species from the gas phase). The positive charge created in the solution within a depth of ~λ_{se} is compensated, and, indeed, no charge effect is observed: the binding energy of aliphatic contamination C 1s peak is seen at 284.80 eV, taking the Fermi level of the gold substrate as the binding energy reference.

As secondary electrons are emitted away from the droplet surface (within a layer of ~λ_{se} depth), negative charges are supplied at the gold/solution interface to maintain neutrality. This means that species are reduced at the metallic electrode, H_2O (to H_2) or the radiolytic species produced in the irradiated depth d_{ir} e.g. H_2O_2 (to HO^-) or IO^- (to I_2), see below. All these reduction reactions produce HO^- ions.

Binding energy reference.

The Fermi level of the gold substrate is used as the zero point for binding energies in the NaCl, NaBr, and NaI solutions. The alignment of electronic levels at the metal/solution interface has been discussed previously in references 14 and 31.

However, for the MgAl-Cl-LDH sample, the scale of binding energies is related to the Mg^{2+} 2p core-level binding energy, which is set at 50.0 eV. This is because the Au 4f doublet was not accessible for measurement. As a result, there is a shift in binding energy of about -1 eV, relative to the Fermi level alignment of the Au in the NaX solutions. We have retained this reference to maintain consistency with the recent paper on hydrated LDH.[17]

RESULTS AND DISCUSSION

NaI aqueous solution

In Figure 4, we display the I 4d spectra of the NaI saturated solution formed at $P_w = 8$ mbar and T = 278 K. Measurements were made in the 200−1200 eV energy interval. The spectra remained unchanged during their accumulation (10 scans of 6 min each). Two measurement runs were performed (run#1 and #2). This allows the analysis of sufficient data to avoid establishing false correlations.

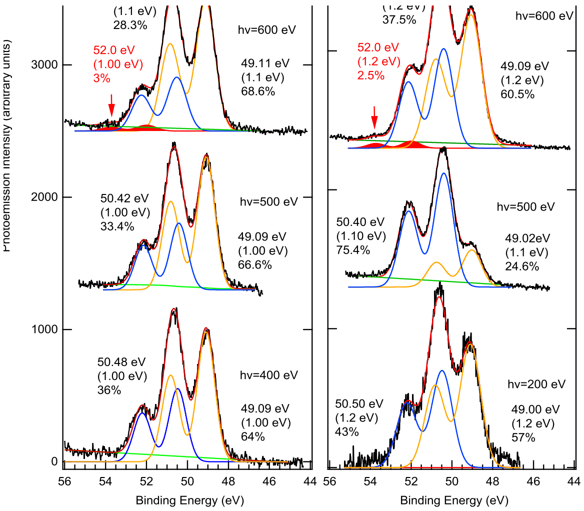

Figure 4. I 4d spectra of the NaI saturated solution surface (P_w = 8 mbar, T = 278 K) during run#1 and run#2. Each doublet is the sum of the $4d_{5/2}$ and $4d_{3/2}$ components. The orange (LBE)

and blue (HBE) doublets are ascribed to I^- and IO^-, respectively, and the red-shaded doublet is a gas phase component (see text). Fit parameters are given: I $4d_{5/2}$ binding energy, Gaussian full-width at half maximum (between parentheses) and spectral weight (%). The binding energy is referenced with respect to the Fermi level of the gold substrate. $\dot{D}_w$ is ~5 10^7 $Gy{\cdot}s^{-1}$ at 200eV, ~10^6 $Gy{\cdot}s^{-1}$ at 400 and 500 eV, 4 10^7 $Gy{\cdot}s^{-1}$ at 600 eV and 10^5 $Gy{\cdot}s^{-1}$ at 1200 eV.

All I 4d spectra are fitted with two main (1.73 eV spin-orbit split) doublets, the low binding energy (LBE) doublet (I $4d_{5/2}$ at 49.1 eV) and the high binding energy (HBE) doublet (I $4d_{5/2}$ at 50.4 eV). The LBE doublet is ascribed to the solvated I^- ion. The HBE doublet corresponds to a radiolytic end product. Moreover, a small feature is discernible at 53.7 eV to the left of the $4d_{3/2}$ flank of the HBE doublet (indicated by the red arrow in Figure 4). It is better seen in the well-accumulated spectra measured at hν=600 eV during run#2 (the measurement is optimized at this energy because of the high photon flux, see Table 1, and a reduced signal attenuation by the gas phase due to the relatively high kinetic energy of ~550 eV). Auger peaks (Xe $M_4N_{45}N_{45}$ at a kinetic energy of 546 eV[35]) or photoelectron peaks (Fe 3p at ~54 eV[35]) can be ruled out. In reality, this component arises from a gaseous species, i.e. the I $4d_{3/2}$ component of the red-shaded doublet, with its companion, the I $4d_{5/2}$ component, at a binding energy of 52.0 eV. Considering that the work function of the solution is ~5 eV,[14] the I $4d_{5/2}$ ionization energy (measured relative to the vacuum level) is around 57 eV. The gas-phase $4d_{5/2}$ ionization energy of I_2 falls within the 57.2-57.5 eV range.[36] It is also possible that the observation of gas phase diiodine at hν = 600 eV is due to the very high dose rate (4 × 10^7 $Gy{\cdot}s^{-1}$) at this energy (above the O K edge).

As shown in the SI, section S3.1, the partial pressure P_I of this iodine-containing gaseous species can be estimated from the gas phase/liquid phase intensity ratios of the I 4d and O 2s core-levels. For a water pressure P_w of 8 mbar, the iodine gas phase pressure is $\sim \frac{0.012}{n}$ mbar, where n is the number of iodine atoms per molecule. Therefore, for I_2 released in the gas phase the partial pressure P_{I_2} would be $\sim 6\times10^{-2}$ mbar.

The I 4d spectra reveal the presence of the HBE doublet across *all* measurements performed in the 200-1200 eV photon energy interval. Its spectral weight spans the 13%-73% interval, as shown in Figure 4 and Figure 5(a). The HBE spectral weight also demonstrates variability between the different experimental runs (more radiolytic species form in run#2 than in run#1). In run#1, a decrease in HBE weight is observed with an increase in photon energy. A simplistic interpretation could attribute this to the photoelectron escape depth effect, as λ_{pe} varies from ~1.4 nm to ~8 nm in the photon energy interval 200−1200 eV.[34] This could suggest that the HBE species accumulates at the gas/liquid interface. However, run#2 contradicts this hypothesis, demonstrating a substantial increase in HBE weight when photon energy is increased from 200 eV to 500 eV. Indeed, as the HBE doublet species is a radiolytic product, interpretations centered on "escape-depth" effects[12] must be reassessed. Indeed, the variability of the dose rate $\dot{D}_w$ with photon energy should directly affect the concentration of HBE, complicating any simple interpretations.

We plot in Figure 5(b) the HBE weight against $\dot{D}_w$ (note the log scale). As we have no evidence for the surface propensity of the radiolytic product, we can admit a constant concentration profile during each measurement. Under this assumption, the pattern we get suggests that the concentration of radiolytic HBE species strongly increases for $\dot{D}_w > 10^6$ Gy·s^{-1}. Nonetheless, unrecognized factors (droplet hydrodynamics, mass transport etc.) and insufficiently controlled parameters (droplet size, halide concentration) cause data scatter, which prevent us to firmly correlate the spectral observable (the HBE weight) with the only experimental parameters we have (photon flux, energy and dose rate). Additional examples of these complexities will be given in the study of the NaI and NaCl solutions.

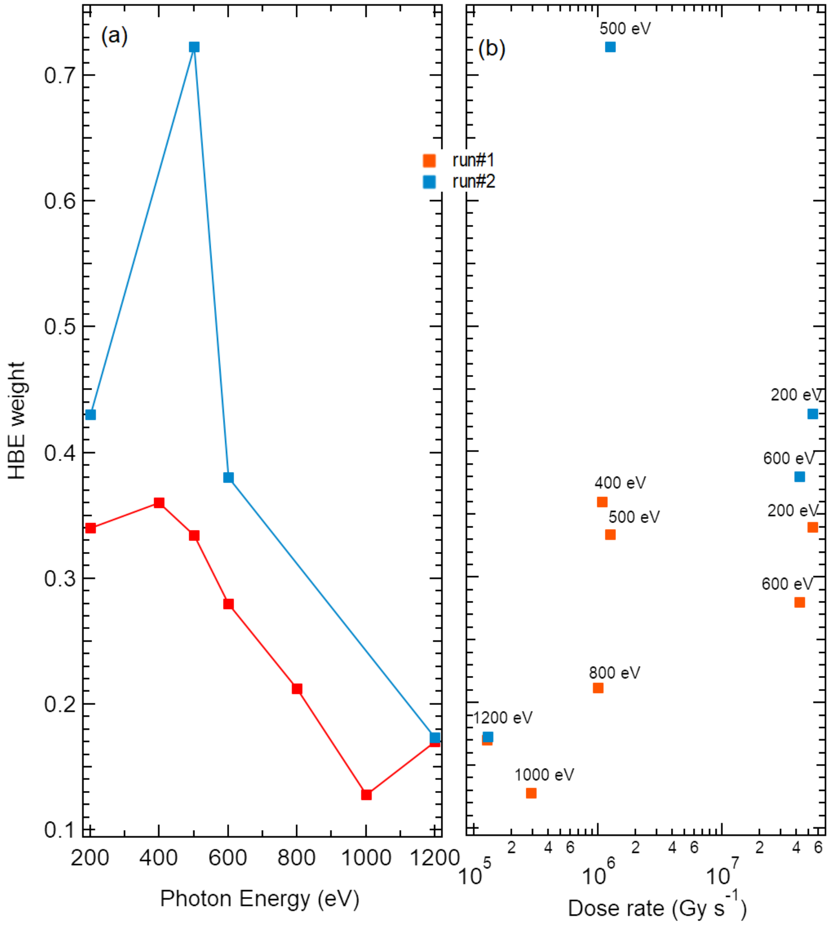

Figure 5. I 4d HBE weight (radiolytic product) plotted against photon energy and dose rate for run#1 and #2, as determined from spectra shown in Figure 4.

We now discuss the attribution of the HBE doublet. Shifted by +1.4 eV with respect to the LBE I^- doublet, this radiolytic product could be attributed to different types of species.

One possibility to consider is that $I^\bullet$ radicals, formed in the solution, are scavenged by organic compounds adsorbed on the surface, resulting in the formation of C-I bonds. Although no I 4d binding energies have been reported for the C-I bond in the NIST XPS database,[35] data for the I $3d_{5/2}$ core level do exist. In this case, the binding energy of C_2H_5I adsorbed on Ag is found to be 2.2 eV higher than that of I^- in solid NaI. This energy difference is significantly larger than the +1.3 eV difference we measure here between the two doublets. We examine in the SI, section S3, whether this HBE weight is correlated with the C 1s spectral shape and intensity. The conclusion is negative. Thus, we find no compelling evidence in favor of the C-I compound hypothesis.

We then explore iodine species having an oxidation state greater than −1, and thus a positive binding energy shift with respect to the I^- doublet.

First, the HBE doublet cannot be attributed to $I_{2(aq)}$ (oxidation state=0), admitting that the gaseous species is $I_{2(gas)}$ and that its partial pressure is 6 10^{-2} mbar (6 Pa). At 298.15 K the Henry's law constant for I_2 is 2.8×10^{-2} mol m^{-3} Pa^{-1}, which is extrapolated to 7.2×10^{-2} mol m^{-3} Pa^{-1} at 278 K using the van 't Hoff equation.[37] This gives a concentration of dissolved $I_{2(aq)}$ of $\sim4\times10^{-4}$ mol L^{-1}. This quantity is not appreciable in the I 4d spectra, considering a total iodine atom concentration in the 1 mol L^{-1} range.

Second, we turn to the triiodide species I_3^-. For symmetric I_3^-, the negative charge (-1) is distributed on the two side atoms which contribute to the LBE doublet, while the central atom contributes to the HBE doublet. The binding energy shift between the two doublets is 1.1 eV (in ethanol[13]), which is compatible with the 1.3 eV shift measured here. An HBE:LBE distribution of 33:66 should be found for triiodide, but the proportion we find for the spectrum measured at 500 eV during run#2 is 73:27 which makes the triiodide attribution incompatible with the experiment. Moreover, the component we see at 53.7 eV is a gas phase component which should not be confounded with the shake-up[13] observed in I_3^- and shifted by +5.2 eV from the LBE component (the side atoms).

We finally consider IO_n^- species (n=1,2,3). An LJ-XPS measurement of IO_3^- (oxidation state=+5) in solution reveals that the 4d doublet is shifted by +5.3 eV compared to I^- (Roose et al.[38]). This value is significantly larger than the +1.3 eV shift we measure here. To our knowledge, no published LJ-XPS measurements exist for the I 4d binding energies of hypoiodous acid IOH and hypoiodite IO^- (oxidation state +1) in water. We can only hypothesize about the binding energy shifts of IO_n^- species compared to I^-. Our assumption can be based on data from the other XO_n^- species binding energies (I 4d, Br 3d, Cl 2p) measured in aqueous solution using LJ-XPS.[38,39,40]

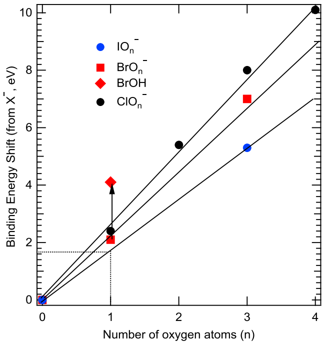

Figure 6. Binding energy shifts of the XO_n^- species (I 4d, Br 3d, Cl 2p) with respect to X^- plotted against n. The binding energy shift of BrOH is also given. Values collected from LJ-XPS experiments.[38,39,40]

We plot in Figure 6 the binding energy shifts of the XO_n^- species relative to the corresponding halide X^- against the number of oxygen atoms *n*. A linear behavior is observed for BrO_n^- and ClO_n^-. For IO_n^- we have only one value (IO_3^-). If we admit that the same linear relation with *n* is valid for IO_n^-, then the I 4d binding energy shift of IO^- with respect to I^- should be 1.6 eV. A chemical shift per O atom smaller for the I atom than for the Br and Cl ones seems reasonable, as I is the biggest of the halogen series and binding energy shifts scale approximately with the inverse of the atomic radius.[41] Then the chemical shift of +1.4 eV we measure is close to the +1.6 eV shift we hypothesize for IO^-. By analogy with the BrOH case (see Figure 6), the binding energy shift of IOH with respect to I^- should be significantly larger than this value. Thus, IOH should be absent.

The assignation of the HBE component in the I 4d spectra to IO^- (Figure 4) does not align with previous radiolysis studies at natural pH which indicate I_3^- as the ultimate product.[21,24] The reaction scheme proposed by Balcerzyk et al.[21] for Br (reported in Figure 1, as a sequence of blue arrows) considers that the $X_2^{\bullet-}$ species is a precursor to X_3^-. However, at alkaline pH the final products are different, as already mentioned in the introduction. Buxton et al.[26] consider reactions leading to $X_{2(gas)}$ ($I_{2(gas)}$) (the red lines in Figure 1) and the subsequent hydrolysis equilibria (K1 and K2). IOH/IO^- are the ultimate radiolysis products at alkaline pH. Speciation curves for $[\Sigma(I_2)]=0.3$ mol L^{-1} with $[I^-]=0.1$ mol L^{-1} given by Truesdale et al.[42] show that IO^- predominates over I_3^-, HOI and I_2OH^- at pH values greater than 12.5. Therefore, the assignment of the I 4d HBE doublet to IO^- means that the pH has significantly increased above 7 under irradiation (at least in the outer layers of the solution probed by photoemission).

X	$K_{X_{2(aq)}}^{XOH}$ $X_{2(aq)} + H_2O \rightleftharpoons XOH + H^+ + Cl^-$	pK_a XOH/XO^-	$K_{X_{2(aq)}}^{XO^-}$ $X_{2(aq)} + 2OH^- \rightleftharpoons XO^- + X^- + H_2O$
I	-	10.4 ($^\heartsuit$)	1.65 10^5 (*$^\spadesuit$)
Br	5.8 10^{-9} ($^\#$)	8.65	1.3 10^{11} ($^\spadesuit$)
Cl	4 10^{-4} ($^\clubsuit$)	7.5	1.3 10^{17} ($^\spadesuit$)

Table 2. $X_{2(aq)}$ hydrolysis equilibrium constants $K_{X_{2(aq)}}^{XOH}$ and $K_{X_{2(aq)}}^{XO^-}$ and XOH pK_a at 25°C. (*) from ref [26] and ($^\spadesuit$) assuming that the water dissociation equilibrium constant K_w is 10^{-14}. ($^\#$) from ref [43]. ($^\clubsuit$) from ref [44]. ($^\heartsuit$) from ref [45].

The equilibrium constant $K_{I_2}^{IO^-}$ of the hydrolysis reaction of aqueous diiodine at alkaline pH

$$I_{2(aq)} + 2HO^- \rightleftharpoons IO^- + I^- + H_2O \qquad \{R1\}$$

is simply equal to $K_{I_2}^{IO^-}=K_1K_2K_3$ (see Figure 1), where $K_1K_2=41.5$[26] at 25°C and $K_3=K_a/K_w$ where $K_a=10^{-pKa}$ is the acid dissociation constant ($pK_a=10.4$ at 25°C[45]) and K_w the water dissociation equilibrium constant (10^{-14} at 25°C). Then the equilibrium constant $K_{I_2}^{IO^-}$ (25°C) of {R1} is 1.65×10^5.

With X being a generic halide, the HO^-concentration $[HO^-]$ is:

$$[OH^-] = \sqrt{\frac{[X^-][XO^-]}{K_{X_2}^{XO^-}[X_{2(aq)}]}} \qquad (1)$$

and

$$pOH = \frac{1}{2}\left(-\log([X^-]) - \log([XO^-]) + \log\left(K_{X_2}^{XO^-}\right) + \log\left([X_{2(aq)}]\right)\right) \qquad (2)$$

Taking [I^-], [IO^-] and [$I_{2(aq)}$] of ~1, ~1 and ~4 10^{-4} mol L^{-1}, respectively (see above), one finds that pOH is 0.4, thus the pH is very high, 13.6. Let us now revisit Figure 1 to understand why the surface layers of water could become alkaline starting from a neutral pH.

Let us first consider the black frame in Figure 1. Pulse radiolysis simulations[46] demonstrate that the pH of *pure* water initially becomes highly acidic due to the reaction of H_2O^+ reacts with H_2O to produce H_3O^+ (plus $HO^\bullet$), and then reverts to neutral (pH 7) in less than 1 μs. This is attributed to the recombination of solvated electrons either with $HO^\bullet$ radicals to yield HO^- ions– the most probable reaction – or directly with H_3O^+ – the less probable reaction – to yield H_2O and a the $H^\bullet$ radical.[47,48] Consequently, H_3O^+ is either neutralized by HO^- or by a solvated electron. In pure water the pH should remain neutral.

The situation changes in halide solutions, if hydroxyl radicals are produced, as they react with X^- to give the $XOH^{\bullet-}$ radical anion, a key intermediate (the $HO^\bullet$ yield was recently determined in pure water using SR,[19] but to our knowledge not in halide solutions). As shown in the green frame of Figure 1, an H_3O^+ cation is consumed to form a halogen atom radical ($X^\bullet$) by reacting with $XOH^{\bullet-}$, or $XOH^{\bullet-}$ decomposes into $X^\bullet$ plus OH^-. Hence, the pH increase. This path is possible if the H_2O^+ precursor does not only react with halide ions (right branch in Figure 1), as stated in ref [21], but also with water molecules (left branch).

pH modifications in halide solutions under γ irradiation are reported by Jung at al.[24] and Kim et al..[25] These authors consider the reaction $2I^- + 2\cdot HO^\bullet + 2H^+ \rightarrow I_{2(aq)} + 2H_2O$,[25] that also consumes protons, to explain why the pH of NaI solutions increases under gamma irradiation when the initial pH is < 7 (note that the above reaction is a condensate of the multiple intermediary reactions leading to $I_{2(aq)}$ depicted in Figure 1). However, at neutral and higher pH the same authors consider that H_2O_2 acts as a reducer ($I_{2(aq)} + H_2O_2 \rightarrow 2I^- + 2H^+ + O_2$). Thus, the contribution to pH changes of I_2 reduction cancels that of I^- oxidation. Therefore, we must admit that in our case potential reducers like H_2O_2 and O_2^- are not present in great quantities, which can be explained by the fact that water is fully deaerated in the vial.[49]

Other hypotheses could also be considered to explain the pH increase. The decrease in the quantity of I^- due to the formation of $I_{2(aq)}$ in the irradiated volume may increase the pH: fewer I^- anions result in the creation of OH^- to equilibrate the charges. However, this is only true if I^- ions from outside the irradiated volume take a significant amount of time to penetrate the irradiation volume. The latter one is a cylinder with a depth (d_{ir}) of ~1 μm and a cross-sectional area of ~10^{-2} mm^2. Since d_{ir} << diameter of the spot, we can calculate the characteristic diffusion time for I^- to penetrate the irradiated volume over a distance d_{ir}: $\tau = (d_{ir})^2/D$. The diffusion coefficient D for I^- is 1.6×10^{-5} cm^2 s^{-1} at 18°C.[50] Therefore, τ is equal to 6.25×10^{-4} s, indicating a very rapid equilibration by sending I^- ions from the non-irradiated zone. Therefore, the iodide depletion hypothesis leading to a pH increase is not realistic.

Figure 2(b) also suggests that the system exhibits characteristics similar to an electrolytic cell, where oxidation takes place at the water/vapor interface, resulting in the production of I_2, while reduction occurs at the metal/solution interface generating H_2 and OH^-. The characteristic time required for OH^- ions produced at the interface to reach the surface, over a distance of ~1 mm (the droplet diameter), is approximately 600 s. This duration is quite significant, considering that in the NaI case the establishment of a steady-state hypoiodite/iodide steady-state concentration ratio appears to occur instantly. Additionally, due to the complex nature of the studied system (droplets), it is exceedingly challenging to calculate the increase in OH^-

concentration at the surface due to reduction reactions at the Au/solution interface. We can only state that a sample current of approximately 1.6 nA yields the generation of 10^{10} OH^{-} ions per second at the gold electrode. To test the "electrolysis" hypothesis, we have plotted of the HBE (IO^{-}) weight against the sample current (run#1) in Figure S4 of the SI. We see no linear correlation, and we cannot draw any conclusive evidence from it.

NaBr aqueous solution

In Figure 7 (a) we present the evolution of the Br 3d spectra with the number of scans (one scan takes 75 s) for an acquisition made at hν = 200 eV, the photon energy at which $\dot{D}_w$ is as high as 5 10^{7} Gy·s^{-1} (see Table 1). All spectra are fitted with two (1.04 eV spin-orbit split) doublets, a first one at 68.1 eV (the LBE doublet) we attribute to bromide Br^{-} and a second one (the HBE doublet) positioned at 69.7 eV, i.e. +1.61 eV to higher binding energy than the Br^{-} doublet. The positive chemical shift indicates that bromine is in an oxidation state greater than −1. As seen in Figure 6(a), the spectrum evolves with time (scan #0 corresponds to the start of X-ray irradiation).

The LBE and HBE doublet respective intensities, as well as the total Br 3d spectrum intensity, are plotted in Figure 7(b) against the number of scans. The total Br 3d intensity diminishes with increasing measurement time. This is entirely due to the intensity decrease of the HBE doublet as, for its part, the LBE doublet (Br^{-}) intensity remains constant with time. As shown in Figure 6(b'), the HBE peak spectral weight of scan #0 is 72 %, while it is only 28 %. for scan #5. The same time evolution (see SI section S5, Figure S5(a)) was observed for the Br 3d core-level measured at hν=600 eV ($\dot{D}_w$ is also in the 10^{7} Gy·s^{-1} range). At this photon energy, the C 1s spectrum (presented in Figure S5(b)) was acquired after displacing the X-ray spot. Contrary to

Br 3d spectra, the C 1s spectrum does not change at all, which eliminates the hypothesis of a correlation between the HBE doublet and thus does not lend support to the formation of a C-Br bond. Figure 7(c) shows the Br 3d spectrum acquired at hν=1000 eV. During this measurement the HBE:LBE intensity distribution remained fairly constant (31:69) of the spectral weight, over 10 scans, i.e. 750 s), in contrast to the observations made at 200 and 600 eV. The HBE component weight at 1000 eV is close to that obtained at hν=200 after 375 s of exposure (scan #5, see Figure 7(b')). Such an observation hinders any attempt to profile the HBE species concentration as a function of depth by changing the photoelectron kinetic energy (and escape depth).

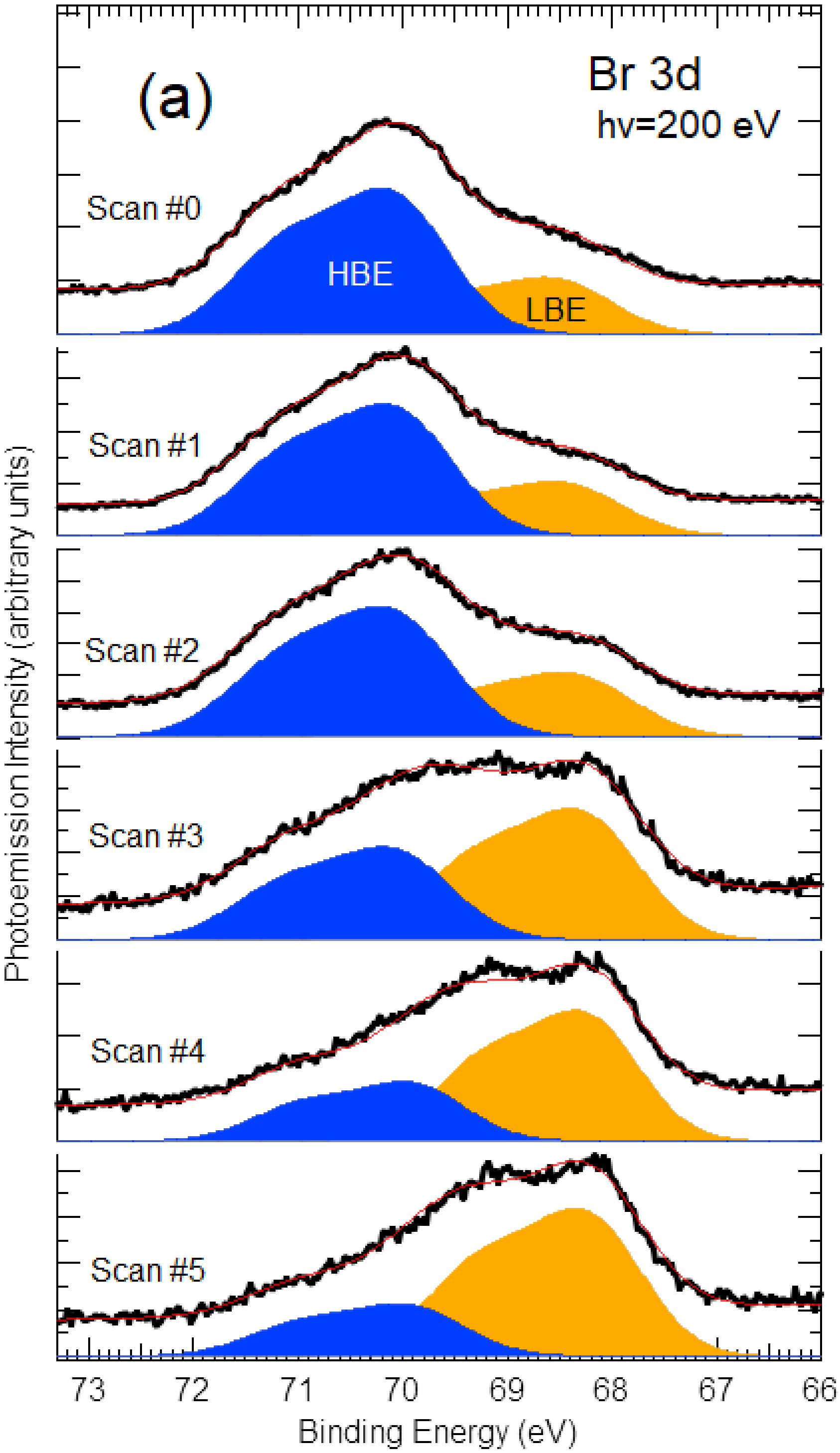
(a)
Br 3d
hv=200 eV
Scan #0
HBE
LBE
Scan #1
Scan #2
Scan #3
Scan #4
Scan #5
Photoemission Intensity (arbitrary units)
73
72
71
70
69
68
67
66
Binding Energy (eV)

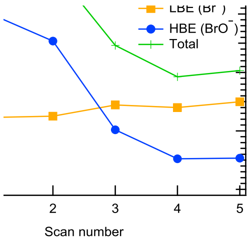
LBE (Br⁻)
HBE (BrO⁻)
Total
2
3
4
5
Scan number

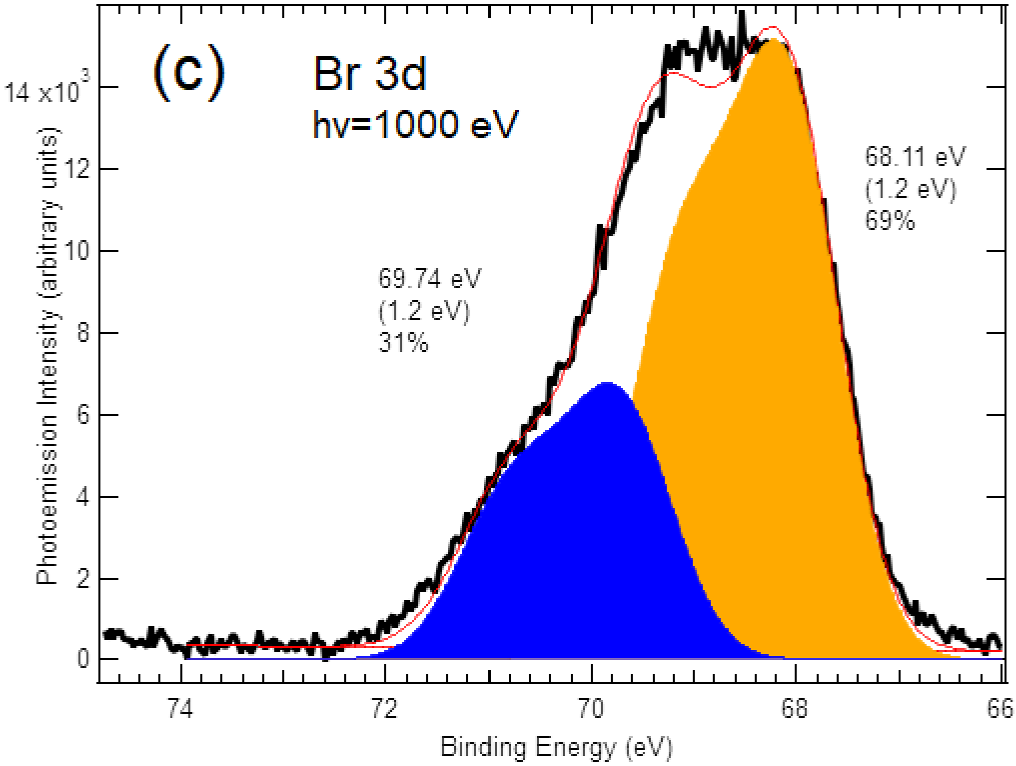

Figure 7. (a) Five successive Br 3d scans of the NaBr saturated solution (P_w= 8 mbar, 278 K) measured at hν = 200 eV (1 scan = 75 s). Each doublet is the sum of the $3d_{5/2}$ and $3d_{3/2}$ components. The orange (LBE) and blue (HBE) doublets are ascribed to Br^- and BrO^-, respectively. (b) plot of the LBE and HBE doublet intensities against scan number (hν = 200 eV). (b') plot of the LBE and HBE spectral weights against scan number (hν = 200 eV). (c) Br 3d spectrum measured at hν = 1000 eV (sum of 10 scans, 750 s). The fit parameters are also given: Br $3d_{5/2}$ binding energy, Gaussian full-width at half maximum (between parentheses) and spectral weight (%).The binding energy is referenced with respect to the Fermi level of the gold substrate. Dose rates are 5 10^7 Gy·s^{-1} and 3 10^5 Gy·s^{-1} at photon energies of 200 and 1000 eV, respectively.

To what species the HBE doublet could be ascribed? Inspection of Figure 6, where data from Gladich et al.[39] are reported, shows that HBE doublet can be attributed to the hypobromite BrO^- (oxidation state +1). No BrO_n^- species with $n>1$ is observed.

In contrast, conventional pulsed radiolytic studies point to the formation of tribromide. Under pulsed γ-irradiation Br_3^-, H_2, and H_2O_2, are produced in the long-time scale.[21] Pulsed (electron) radiolysis studies also point to tribromide, stable at pH values below 4.[51] In reality, the tribromide hypothesis is in contradiction with the spectroscopy data of Figure 7. We can use the same argument as for triiodide to demonstrate it. Assuming a symmetric Br_3^-, and attributing the HBE doublet to the central atom and the LBE one to the two side atoms (coincident with bromide binding energy) gives an HBE:LBE intensity distribution of 33:66. This is obviously inconsistent with the fact that the LBE doublet intensity is smaller than that of the HBE one for scans # 0, 1 and 2 of the spectra acquired at hν = 200 eV. Naturally, the time variations of the HBE:LBE intensity distribution hinder a photon-energy dependent study aimed at determining the depth distribution of the species.

The fact that Br_3^- is not seen also suggests that, like the NaI case, $Br_{2(aq)}$ is hydrolyzed to BrO^- because the solution is basic. This is in line with the absence of BrOH, given that the pK_a of BrOH is 8.65.

We consider the hydrolysis equilibrium of aqueous dibromine at basic pH, as in the NaI case

$$Br_{2(aq)} + 2OH^- \rightleftharpoons BrO^- + Br^- + H_2O \qquad \{R2\}$$

The equilibrium constant $K_{Br_2}^{BrO^-}$ is 1.3×10^{11} at 25°C (Table 2), 6 orders of magnitude greater than $K_{I_2}^{IO^-}$, which means that BrO^- can be the dominant species at lower pHs than IO^-. We do not identify $Br_{2(gas)}$ in the NAP-XPS spectrum, contrary to the NaI case. The $3d_{5/2}$ ionization energy of gas phase Br_2 (vacuum level reference) is 77.4 eV,[36] which would give a Br $3d_{5/2}$ (Br $3d_{3/2}$)

binding energy in the 72.4 eV (73.4 V) range with respect to the gold Fermi level, considering the work function of ~5 eV. As we see nothing in this region, this means that the partial pressure of the gas phase species is below the detection limit of NAP-XPS we estimate to be 10^{-2} mbar (1 Pa). This means that [$Br_{2(aq)}$] is below 7×10^{-3} mol m^{-3} (7 10^{-6} mol L^{-1}) considering a Henry's law constant of 7.2×10^{-3} mol m^{-3} Pa^{-1}. Using equation (2), and [BrO^{-}], [Br^{-}] and [$Br_{2(aq)}$] of ~ 1 mol L^{-1}, 1 mol L^{-1} and 7 10^{-6} mol L^{-1}, respectively, pOH <3. This means that the pH can be greater than 11. It is also clear that BrO^{-} does not disproportionate to bromide and bromate (the binding energy of the BrO_3^{-} doublet is shifted by 7.2 eV from that of Br^{-}, see Figure 6).

The reason why the HBE:LBE distribution evolves with time remains unclear. The fact it is seen at 200 et 600 eV (when the dose rate is maximum) and not at 1000 eV, may suggest a dose rate threshold effect.

NaCl aqueous solution

In Figure 8, we present a collection of four Cl 2p spectra obtained from a NaCl solution. These spectra were recorded at photon energies of 500 eV and 1200 eV. The dose rate is observed to be approximately one-tenth of its value at 500 eV when measured at 1200 eV. Irrespective of the photon energy, each Cl 2p spectrum is characterized by two (1.61 eV spin-orbit split) doublets. The LBE doublet (Cl $2p_{3/2}$ binding energy at ~198.5 eV) is attributed to Cl^{-}. The HBE doublet (Cl $2p_{3/2}$ at ~200.6 eV) is shifted by +2.1 eV relatively to the Cl^{-} doublet. Despite increasing acquisition times, the spectra remained unchanged. However, upon reanalyzing the data, we noted a significant variation in the HBE:LBE distribution, depending on the measurement position, even at a constant photon energy (and dose rate). Figure 8 illustrates this observation, suggesting that the steady-state concentration might be influenced not only by $\dot{D}_w$ but also by other parameters. Specifically, at a photon energy of 500 eV, a larger droplet exhibits a greater HBE spectral weight than a smaller one. This observation may indicate a correlation between the HBE:LBE distribution and the concentration, or the solution hydrodynamics, which could vary according to droplet size. Further investigation is necessary to clarify this point, with the first step being a better control of volumes and solute concentrations. The scatter of the HBE:LBE intensity distribution in Figure 8, which complicates any interpretation in terms of escape depths and dose rates, raises questions about the surface propensity of the HBE species suggested in prior studies.[11,12]

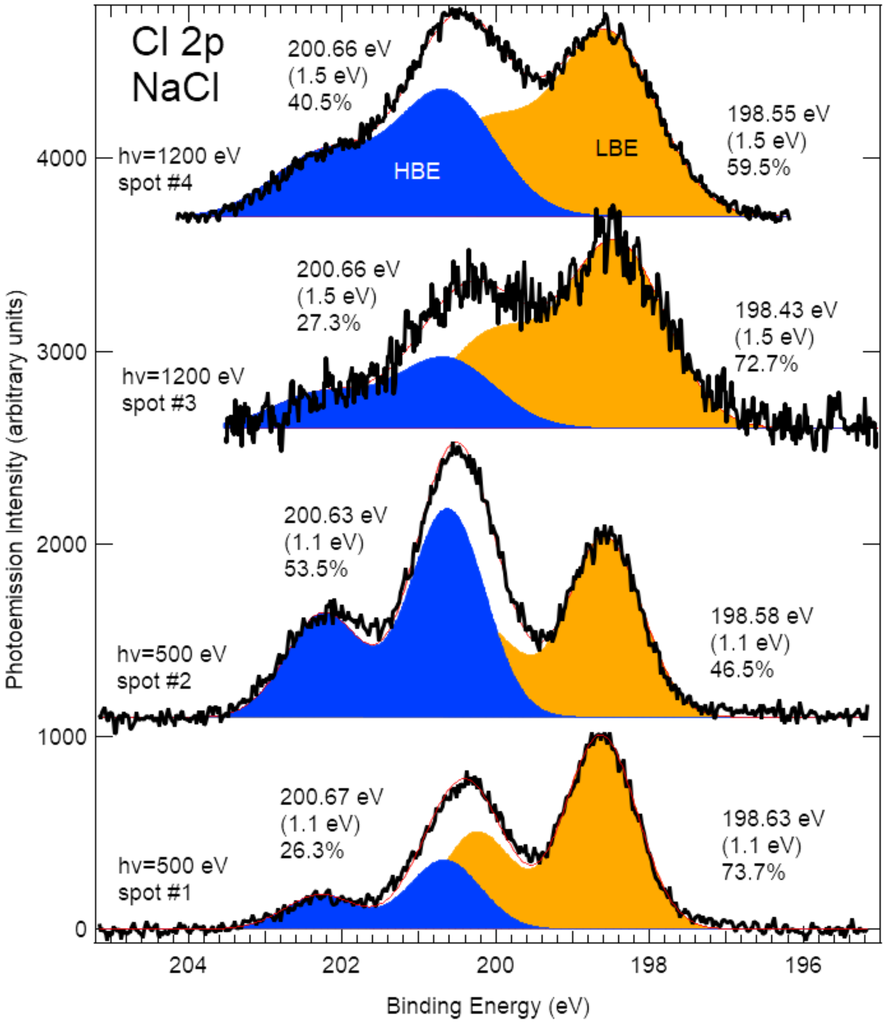

Figure 8. Cl 2p NAP-XPS spectra of the NaCl solution (P_w= 8 mbar, 278 K) acquired at hν= 500 eV and 1200 eV. Different spots are explored on the sample. Spot #2 corresponds to a much bigger droplet than spot #1. The doublets are the sum of the $2p_{3/2}$ and $2p_{1/2}$ components. The orange (LBE) and blue (HBE) doublets are ascribed to Cl^- and ClO^-, respectively. The fit parameters are also given: Cl $2p_{3/2}$ binding energy, Gaussian full-width at half maximum (between parentheses) and spectral weight (%).The BE is referenced with respect to the Fermi level of the gold substrate. Dose rates are ~10^6 Gy·s^{-1} and ~10^5 Gy·s^{-1} at photon energies of 500 and 1200 eV, respectively.

We found no correlation between the relative intensity of the HBE doublet and the C 1s shape and intensity (refer to SI, section S6, Figure S6), ruling out the formation of C-Cl bonds. Therefore, the HBE species is a ClO_n^- species. Using the LJ-XPS binding energies of ClO_n^- anions in water,[40] as seen in Figure 6, we attribute the HBE doublet to ClO^- (2.4 eV higher in energy that the Cl^- doublet). ClOH is disregarded as the addition of a proton to the base significantly increases the binding energy (consider the $BrOH/BrO^-$ Br 3d binding energy difference of +2 eV, as shown in Figure 6, and the N 1s binding energy difference of the HNO_3/NO_3^- couple which is 1 eV[52]). Given that the pKa of the $ClOH/ClO^-$ couple is 7.5, we should observe both the acid and its conjugated base at neutral pH. This is not the case in our observations, suggesting that the pH becomes basic under irradiation.

As seen with iodide and halide solutions, we can also explain the formation of the hypochlorite ion by the formation of aqueous dichlorine) under soft X-ray beam irradiation, followed by hydrolysis in a basic solution. At alkaline pH, the disproportionation of $Cl_{2(aq)}$ is:

$$Cl_{2(aq)} + 2OH^- \rightleftharpoons ClO^- + Cl^- + H_2O \qquad \{R3\}$$

The equilibrium constant $K_{Cl_2}^{ClO^-}$ of {R3} can be calculated using available thermodynamic data and is found equal to 1.3 10^{17} at 25°C (see Table 2). $[Cl_{2(aq)}]$ can be estimated considering a partial pressure of $Cl_{2(gas)}$ below 10^{-2} mbar (1 Pa), the detection limit (we see no gas phase signal in the NAP-XPS spectra). Using a Henry's law constant of 9.2×10^{-4} mol m^{-3} Pa^{-1},[37] $[Cl_{2(aq)}]$ is below 9.2 10^{-4} mol m^{-3} (9.2 10^{-7} mol L^{-1}). With $[Cl^-]$, $[ClO^-]$ equal to 4 and 2 mol L^{-1}, respectively, and $[Cl_{2(aq)}] < 9.2\ 10^{-7}$ mol L^{-1}, and using equation (2) we find pOH < 5.5. This implies that the pH is greater than ~8.5.

Mg-Cl solution formed over $[Mg_2Al(OH)_6]^+[Cl^-, yH_2O]$ (LDH)

We turn now our attention to the $[Mg_2Al(OH)_6]^+[Cl^-, yH_2O]$ LDH powder and to the water film condensed over it by cooling the substrate to 1°C, under a water vapor pressure P_w of 4.5 mbar. The Cl 2p spectrum of the as synthetized LDH is given in Figure 9(a) in its “dry” state (spectrum acquired using a monochromatized AlK_α source). We see a single 2p doublet, with a Cl $2p_{3/2}$ binding energy of ~197.6 eV characteristic of Cl^-. Note that the binding energy is shifted by -1 eV with respect to the NaCl solution due to a different zero binding energy reference (see METHODS).

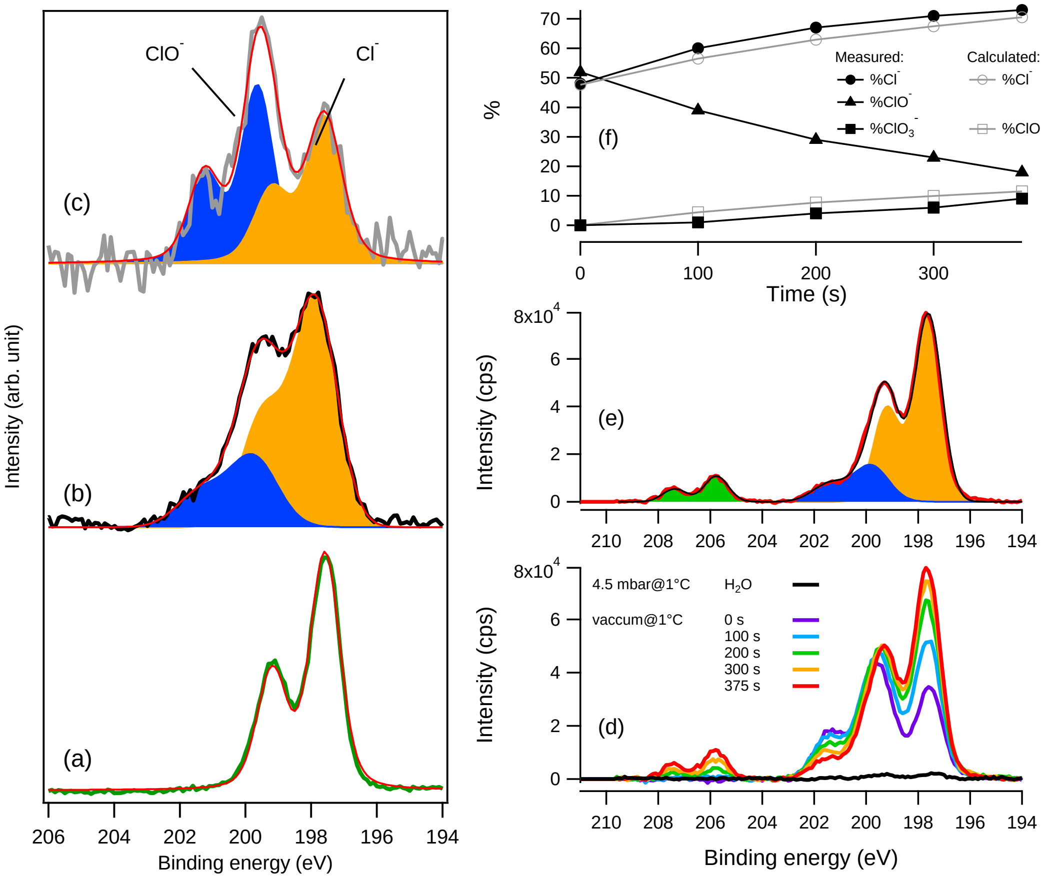

Figure 9. Cl 2p spectra of the $[Mg_2Al(OH)_6]^+[Cl^-]$ LDH and of the Mg-Cl solution formed over it upon water condensation under P_w=4.5 mbar and at 274 K (1°C). The doublets are the sum of the $2p_{3/2}$ and $2p_{1/2}$ components. (a) the "dry' LDH under UHV (monochromatized AlK_α source, hν = 1486.7 eV). (b) the Mg-Cl solution measured with NAP-XPS at hν =1000 eV. (c) same as (b) but measured at hν = 420 eV. (d) the Mg-Cl solution measured with NAP-XPS at hν = 420 eV (the black line represents the spectrum under P_w=4.5 mbar), and the subsequent spectra recorded under vacuum drying (color lines). (e) Fitting of the Cl 2p spectrum at time 375 s. (d) Time evolution under vacuum drying of the Cl^-, ClO^- and ClO_3^- doublet intensities, measured (black filled symbols) and calculated (grey open symbols) from ClO^- intensities assuming the disproportionation reaction $3\ ClO^- \rightarrow 2\ Cl^- + ClO_3^-$. Fitting parameters are given the SI, section S7, Tables S4 and S5.

Additionally, we show in Figure 9(b,c) the NAP-XPS Cl 2p spectrum of the LDH powder covered with a film of water. As already discussed in Coustel et al.[17], a Mg-Cl solution is produced. Indeed, the Al core-levels (2p and 2s) vanish from the NAP-XPS overview scan once the water film appears. The NAP-XPS Cl 2p spectra of the Mg-Cl solution recorded at hν = 1000 and 420 eV, curves (b) and (c), can be fitted by two doublets having with their Cl $2p_{3/2}$ components at ~197.7 eV (LBE) and ~199.6 eV (HBE), respectively. As for the NaCl solution (Figure 8), the LBE $2p_{3/2}$, is attributed to the Cl^- ions, and the HBE doublet, shifted by + 2 eV with respect to the Cl^- doublet is ascribed to ClO^- (see also Figure 6). Thus, the oxidation of the solvated chloride under soft X-ray irradiation depends little on the counter cation, Mg^{2+} or Na^+, and the reaction paths proposed in Figure 1 can also apply to the Mg-Cl solution. For a chlorine-containing LDH at relative humidity between 10% and 75%, the high radiolytic H_2 yield is ascribed by Lainé et al.[53] to the scavenging of $HO^{\bullet}$ by Cl^{-} to give a key intermediate $ClOH^{\bullet-}$ also considered in Figure 1. However, Lainé et al. propose that two $ClOH^{\bullet-}$ recombine:

$2\ ClOH^{\bullet-} \rightarrow 2\ ClO^{-} + H_2$ {R4}

or that $ClOH^{\bullet-}$ scavenges a $H^{\bullet}$ radical:

$ClOH^{\bullet-} + H^{\bullet} \rightarrow ClO^{-} + H_2$ {R5}

Reactions R4 and R5 lead to the formation of the hypochlorite ion and H_2, but they do not result in the production of Cl_2 molecules and HO^{-} ions (as depicted in Figure 1). Consequently, they cannot be accommodated within our explanatory framework of the pH increase.

The relative intensity of the components apparently depends on the photon energy. The spectral weight of the HBE doublet is 52 % at *hv* = 420 eV (curve (c) and only 26 % at 1000 eV (curve (b)). However, due to lessons drawn from the NaCl solution experiment we refrain from discussing a possible surface propensity of the ClO^{-} species.

As long as the solution is in equilibrium with the gas phase, we do not observe the disproportionation of the hypochlorite ion. The situation changes when P_w decreases. The Cl 2p NAP-XPS spectra (Figure 8(d)) were recorded after closing the microvalve connecting the water vial and the analysis chamber and opening the primary pump valve. Then the pressure decreased from 4.5 mbar to 10^{-8} mbar. The black curve corresponds to the Cl 2p spectrum measured under P_w=4.5 mbar *before* evacuating the chamber, and the color ones are measured while pumping.

In NAP-XPS experiments the attenuation of the photoemission intensity due to scattering events in the gas phase, is suppressed for pressures below 0.1 mbar. This explains the strong increase of the photoemission signal in the “time 0 s” spectrum. In this spectrum, the ClO^{-} component still represents 52 % of the Cl 2p spectrum, the same value as that found for the solution under 4.5 mbar. For the subsequent spectra, the overall Cl 2p signal still increases, which is due to *an increase of the Cl concentration* associated to vacuum drying. We observe that the weight of the doublet ascribed to ClO^- decreases while that of the Cl^- doublet increases. Contemporaneously, *a third component shows up, with its Cl 2p$_{3/2}$ component at 206.0 eV*, shifted by +8.2 eV from the Cl^- doublet. This shift is characteristic of the ClO_3^- species (see Figure 6 and ref [40]). Therefore, the evolution of the Cl 2p spectra recorded during vacuum drying of the soaked LDH sample point to the disproportionation of the hypochlorite ion Cl(+1) into Cl(−1) and Cl(+5) species according to:

$3ClO^- \rightarrow ClO_3^- + 2\,Cl^-$ {R6}

The weights of the three doublets were determined from the fitting of the Cl 2p spectra (Figure 9(e)). The analysis is quantitatively consistent with the formation of Cl^- and ClO_3^- with a $[Cl^-]$:$[ClO_3^-]$ ratio of 2:1, as expected from the disproportionation reaction R6.

The disproportionation of hypochlorite is certainly triggered by a strong concentration increase of hypochlorite (decrease of H_2O content) when the brine dries out, as ClO_3^- formation is not observed by NAP-XPS in the Mg-Cl solution under P_w=4.5 mbar. In reality {R4} is decomposed into two consecutive reactions:[54,28]

$2ClO^- \rightarrow ClO_2^- + Cl^-$ {R7} (slow)

$ClO_2^- + ClO^- \rightarrow ClO_3^- + Cl^-$ {R8} (fast)

The rate of the 2nd order rate-limiting reaction R7 involving two hypochlorite molecules will increase with increasing concentration, which will be the case when the sample is dried.

An enhanced methodology for identifying and studying radiolytic effects in aqueous solution with SR NAP-XPS

The results discussed in this paper encourage us to propose an enhanced NAP-XPS methodology aimed at both detecting radiolytic effects in aqueous solutions or studying them because of their specific interest. Several key factors require careful consideration.

Regarding the detection of radiolysis products escaping into the gas phase, integrating mass spectrometry into NAP-XPS measurements can be invaluable in alerting spectroscopists to beam damage, and in deepening our understanding of the radiolytic effects under study. This is not an insurmountable challenge, as manufacturers already offer the option of installing a quadrupole mass spectrometer within the differentially pumped entrance lenses of the analyzer. The sensitivity limit for NAP-XPS detection of gaseous products is about 10^{-2} mbar, as demonstrated here. With an embedded quadrupole mass analyzer, a pressure limit at least two orders of magnitude lower can be achieved.[29]

It is also crucial to accurately measure the photon flux as a function of photon energy (hν) to determine the dose rate. Indeed, if radiolytic effects are present, it is essential to maintain consistent dose rates during comparative measurements at different *hν* (*all other things being equal*) to prevent potential inaccuracies in the results. In this study, the photon flux was determined from the I_0 filament current at the beam entrance. In situ or transportable photodiodes can be also conveniently used. The sample current should also be monitored throughout the study.

A limitation of the current approach, which involves dissolving the salts in droplets with some variation in volume, is an insufficiently precise control of solute concentration. In addition, the hydrodynamics of the droplets complicates the analysis. This could explain the relative scatter of radiolytic species concentrations. Better control can be achieved through the use of customdesigned cells possessing precisely defined volumes and flow-rates. Microfluidic cells could be employed, offering a solution half way between the "fast running" liquid microjets and the current "quasi-static" situation. Partial open flow cells,[55] compatible with high vacuum ($<10^{-7}$ mbar), have already been designed, featuring a hole of only 2–3 μm in diameter on the SiN film window. In the context of a NAP system, the open part could likely be enlarged. Finally, internally monitoring the pH and redox potential in the cell could also significantly enhance our understanding of the phenomena under investigation, but this goal can be technically harder to achieve.

CONCLUSION

The reassessment of NAP-XPS data of halide (I^-, Br^-, Cl^-) solutions provides conclusive evidence that a soft X-ray synchrotron beam causes the oxidation of X^- species into hypohalite XO^-. No alternative (e.g. halocarbons) can explain the body of XPS data. The generated species, IO^-, BrO^-, and ClO^- coexist with their parent ion X^- in comparable concentrations. The gaseous $I_{2(gas)}$ species is identified in the NAP-XPS I 4d spectrum of the NaI solution.

At first glance, the detection of IO^- and BrO^- might seem unexpected, considering a system (solution droplets) presumed to be at neutral pH. Indeed, at pH~7, the stable I_3^- and Br_3^- anions are observed in conventional pulse radiolytic studies. We interpret these observations as due to the hydrolysis of aqueous $X_{2(aq)}$ species at a basic pH. Why the pH would become alkaline in the water layers probed by XPS is a matter of future research. Currently, we speculate that $HO^\bullet$

radicals are produced, despite the high halide concentration, leading to the key intermediate $XOH^{\bullet-}$ whose subsequent reaction will increase the pH.

The steady-state $[XO^-]$:$[X^-]$ distribution does not only depend on the beam conditions (energy and flux), and thus on the dose rate. Some scatter in the $[XO^-]$:$[X^-]$ distribution appears to be due to factors that are not yet fully understood (solute concentration, mass transport, hydrodynamics). In the particular case of the NaBr solution the establishment of a steady-state $[BrO^-]$:$[Br^-]$ ratio could be observed over several minutes, a phenomenon also difficult to explain. This data scatter, combined to the strong dose rate variation with photon energy, hinders any attempt to determine the concentration profile of XO^- by manipulating the photoelectron escape depth.

Neither in NaX solutions, nor in the Mg-Cl solution formed from a Cl-containing LDH, do the hypohalite species undergo disproportionation. Only when drying the Mg-Cl solution and subsequently increasing the concentration, can we monitor the disproportionation reaction of ClO^- into Cl^- and ClO_3^- in real-time.

Building on these observations, this paper proposes guidelines for gaining a more comprehensive understanding of radiolytic effects in solutions, which can enhance the overall success of NAP-XPS studies, especially in fields like environmental chemistry and electrochemistry, where interfaces with liquid water are formed.

ASSOCIATED CONTENT

Supporting Information. In the Supporting Information we provide: the calculation of the photon flux variations with hν, the calculation of the partial pressure of the iodine gaseous species over the NaI solution, the C 1s spectra of the NaI solution, the I 4d HBE weight against sample current, the Br 3d and C 1s spectra of the NaBr solution, the C 1s spectra of the NaCl, and the fitting parameters of the LDH spectra. The following files are available free of charge. SI_NAP_RADIO_JPCC (PDF).

AUTHOR INFORMATION

Corresponding Author

* Héloïse Tissot (email: heloise.tissot@univ-lille.fr)

* Romain Coustel (email: romain.coustel@univ-lorraine.fr)

* François Rochet (email: francois.rochet@sorbonne-universite.fr)

Present Addresses

[†] Institut Rayonnement-Matière de Saclay, Service de Physique de l'Etat Condensé, Laboratoire d'Etude des Nano-Structures et Imagerie de Surface, Commissariat à l’Energie Atomique et aux Energies Alternatives (CEA). 91191 Gif-sur-Yvette cedex, France. Email : boucly.anthony@gmail.com

Author Contributions

FR, HT and RC wrote the manuscript. JJG and FB contributed to the experiments on sodium halide solutions. AB contributed to the experiments on the layered double hydroxide (LDH) material. CC and EA produced and characterized the LDH material. All authors have given approval to the final version of the manuscript.

ACKNOWLEDGMENT

The NAP-XPS experiment, managed by the LCPMR team (Sorbonne Université), was funded by the Ile-de-France Region (Photoémission Environnementale en Ile-de-France, SESAME n°090003524), by the Agence Nationale de la Recherche (Surfaces under Ambient Pressure with Electron Spectroscopies, ANR- 08-BLAN-0096), and by Université Pierre et Marie Curie (now Sorbonne Université). Synchrotron SOLEIL supported the integration of the setup to TEMPO beamline. The authors thank warmly the TEMPO beamline staff for their efficient assistance. Anthony Boucly thanks Région Ile de France for his PhD grant HORS DIM EAU. We thank A. Renard (LCPME-Nancy) for performing the UHV-XPS analysis of the LDH material.

ABBREVIATIONS

LJ, liquid jet, NAP, near ambient pressure, SR, synchrotron radiation, XPS, X-ray photoelectron spectroscopy

REFERENCES

(1) Ogletree, D. F.; Bluhm, H.; Lebedev, G.; Fadley, C. S.; Hussain, Z.; Salmeron, M. A Differentially Pumped Electrostatic Lens System for Photoemission Studies in the Millibar Range. *Rev. Sci. Instrum.* **2002**, *73* (11), 3872–3877.

https://doi.org/10.1063/1.1512336.

(2) Dupuy, R.; Richter, C.; Winter, B.; Meijer, G.; Schlögl, R.; Bluhm, H. Core Level Photoelectron Spectroscopy of Heterogeneous Reactions at Liquid–Vapor Interfaces: Current Status, Challenges, and Prospects. *J. Chem. Phys.* **2021**, *154* (6), 060901. https://doi.org/10.1063/5.0036178.

(3) Frank Ogletree, D.; Bluhm, H.; Hebenstreit, E. D.; Salmeron, M. Photoelectron Spectroscopy under Ambient Pressure and Temperature Conditions. *Nucl. Instruments Methods Phys. Res. Sect. A Accel. Spectrometers, Detect. Assoc. Equip.* **2009**, *601* (1–2), 151–160. https://doi.org/10.1016/j.nima.2008.12.155.

(4) Trotochaud, L.; Head, A. R.; Karslıoğlu, O.; Kyhl, L.; Bluhm, H. Ambient Pressure Photoelectron Spectroscopy: Practical Considerations and Experimental Frontiers. *J. Phys. Condens. Matter* **2017**, *29* (5), 053002. https://doi.org/10.1088/1361-648X/29/5/053002.

(5) Axnanda, S.; Crumlin, E. J.; Mao, B.; Rani, S.; Chang, R.; Karlsson, P. G.; Edwards, M. O. M.; Lundqvist, M.; Moberg, R.; Ross, P.; Hussain, Z.; Liu, Z. Using "Tender" X-Ray Ambient Pressure X-Ray Photoelectron Spectroscopy as A Direct Probe of Solid-Liquid Interface. *Sci. Rep.* **2015**, *5*, 9788. https://doi.org/10.1038/srep09788.

(6) Rotonnelli, B.; Dias Fernandes, M.-S.; Bournel, F.; Gallet, J.-J.; Lassalle-Kaiser, B. In Situ/Operando X-Ray Absorption and Photoelectron Spectroscopies Applied to Water-Splitting Electrocatalysis. *Curr. Opin. Electrochem.* **2023**, 101314. https://doi.org/10.1016/j.coelec.2023.101314.

(7) Boucly, A.; Rochet, F.; Arnoux, Q.; Gallet, J.-J.; Bournel, F.; Tissot, H.; Marry, V.;

Dubois, E.; Michot, L. Soft X-Ray Heterogeneous Radiolysis of Pyridine in the Presence of Hydrated Strontium-Hydroxyhectorite and Its Monitoring by Near-Ambient Pressure Photoelectron Spectroscopy. *Sci. Rep.* **2018**, *8* (1), 6164. https://doi.org/10.1038/s41598-018-24329-8.

(8) Le Caër, S.; Pin, S.; Esnouf, S.; Raffy, Q.; Renault, J. P.; Brubach, J.-B.; Creff, G.; Roy, P. A Trapped Water Network in Nanoporous Material: The Role of Interfaces. *Phys. Chem. Chem. Phys.* **2011**, *13* (39), 17658. https://doi.org/10.1039/c1cp21980d.

(9) Pignié, M.-C.; Shcherbakov, V.; Charpentier, T.; Moskura, M.; Carteret, C.; Denisov, S.; Mostafavi, M.; Thill, A.; Le Caër, S. Confined Water Radiolysis in Aluminosilicate Nanotubes: The Importance of Charge Separation Effects. *Nanoscale* **2021**, *13* (5), 3092–3105. https://doi.org/10.1039/D0NR08948F.

(10) Weatherup, R. S.; Wu, C. H.; Escudero, C.; Pérez-Dieste, V.; Salmeron, M. B. Environment-Dependent Radiation Damage in Atmospheric Pressure X-Ray Spectroscopy. *J. Phys. Chem. B* **2018**, *122* (2), 737–744. https://doi.org/10.1021/acs.jpcb.7b06397.

(11) Cheng, M. H.; Callahan, K. M.; Margarella, A. M.; Tobias, D. J.; Hemminger, J. C.; Bluhm, H.; Krisch, M. J. Ambient Pressure X-Ray Photoelectron Spectroscopy and Molecular Dynamics Simulation Studies of Liquid/Vapor Interfaces of Aqueous NaCl, RbCl, and RbBr Solutions. *J. Phys. Chem. C* **2012**, *116* (7), 4545–4555. https://doi.org/10.1021/jp205500h.

(12) Tissot, H.; Olivieri, G.; Gallet, J.-J.; Bournel, F.; Silly, M. G.; Sirotti, F.; Rochet, F.

Cation Depth-Distribution at Alkali Halide Aqueous Solution Surfaces. *J. Phys. Chem. C* **2015**, *119* (17), 9253–9259. https://doi.org/10.1021/jp512695c.

(13) Eriksson, S. K.; Josefsson, I.; Ottosson, N.; Öhrwall, G.; Björneholm, O.; Siegbahn, H.; Hagfeldt, A.; Odelius, M.; Rensmo, H. Solvent Dependence of the Electronic Structure of I – and I 3 –. *J. Phys. Chem. B* **2014**, *118* (11), 3164–3174. https://doi.org/10.1021/jp500533n.

(14) Tissot, H.; Gallet, J.-J.; Bournel, F.; Olivieri, G.; Silly, M. G.; Sirotti, F.; Boucly, A.; Rochet, F. The Electronic Structure of Saturated NaCl and NaI Solutions in Contact with a Gold Substrate. *Top. Catal.* **2016**, *59* (5–7), 605–620. https://doi.org/10.1007/s11244-015-0530-6.

(15) Brown, M. A.; Lee, M.-T.; Kleibert, A.; Ammann, M.; Giorgi, J. B. Ion Spatial Distributions at the Air– and Vacuum–Aqueous K 2 CO 3 Interfaces. *J. Phys. Chem. C* **2015**, *119* (9), 4976–4982. https://doi.org/10.1021/acs.jpcc.5b00257.

(16) Arima, K.; Jiang, P.; Deng, X.; Bluhm, H.; Salmeron, M. Water Adsorption, Solvation, and Deliquescence of Potassium Bromide Thin Films on SiO 2 Studied by Ambient-Pressure X-Ray Photoelectron Spectroscopy. *J. Phys. Chem. C* **2010**, *114* (35), 14900–14906. https://doi.org/10.1021/jp101683z.

(17) Coustel, R.; Boucly, A.; André, E.; Di Bitetto, A.; Bournel, F.; Gallet, J.-J.; Rochet, F.; Carteret, C. NAP-XPS Probes the Electronic Structure of the Mg–Al–Cl Layered Double Hydroxide upon Controlled Hydration. *J. Phys. Chem. C* **2023**, *127* (8), 4144–4153. https://doi.org/10.1021/acs.jpcc.2c05362.

(18) Le Caër, S. Water Radiolysis: Influence of Oxide Surfaces on H2 Production under Ionizing Radiation. *Water* **2011**, *3* (4), 235–253. https://doi.org/10.3390/w3010235.

(19) Huart, L.; Nicolas, C.; Kaddissy, J. A.; Guigner, J.-M.; Touati, A.; Politis, M.-F.; Mercere, P.; Gervais, B.; Renault, J.-P.; Hervé du Penhoat, M.-A. Soft X-Ray Radiation and Monte Carlo Simulations: Good Tools to Describe the Radiation Chemistry of Sub-KeV Electrons. *J. Phys. Chem. A* **2020**, *124* (10), 1896–1902. https://doi.org/10.1021/acs.jpca.9b10539.

(20) Matheson, M. S.; Mulac, W. A.; Weeks, J. L.; Rabani, J. The Pulse Radiolysis of Deaerated Aqueous Bromide Solutions 1. *J. Phys. Chem.* **1966**, *70* (7), 2092–2099. https://doi.org/10.1021/j100879a004.

(21) Balcerzyk, A.; Laverne, J.; Mostafavi, M. Direct and Indirect Radiolytic Effects in Highly Concentrated Aqueous Solutions of Bromide. *J. Phys. Chem. A* **2011**, *115* (17), 4326–4333. https://doi.org/10.1021/jp2012528.

(22) Karim, A.; Omar, E.; Schmidhammer, U.; Rousseau, B.; Laverne, J.; Mostafavi, M. Competition Reactions of H 2 O •+ Radical in Concentrated Cl − Aqueous Solutions: Picosecond Pulse Radiolysis Study. *J. Phys. Chem. A* **2012**, *116*, 25. https://doi.org/10.1021/jp309381z.

(23) Crawford, E.; McIndoe, J. S.; Tuck, (the late) Dennis G. The Energetics of the X 2 + X – → X 3 – Equilibrium (X = Cl, Br, I) in Aqueous and Nonaqueous Solution. *Can. J. Chem.* **2006**, *84* (12), 1607–1613. https://doi.org/10.1139/v06-165.

(24) Jung, S.-H.; Yeon, J.-W.; Hong, S. Y.; Kang, Y.; Song, K. The Oxidation Behavior of

Iodide Ion Under Gamma Irradiation Conditions. *Nucl. Sci. Eng.* **2015**, *181* (2), 191–203. https://doi.org/10.13182/NSE14-87.

(25) Kim, M.; Hong, S. Y.; Kim, T.; Jung, S.-H.; Yeon, J.-W. Change in the PH of NaI and Methyl Alkyl Ketone Solutions under Gamma Irradiation. *J. Radioanal. Nucl. Chem.* **2020**, *326* (1), 121–127. https://doi.org/10.1007/s10967-020-07346-8.

(26) Buxton, G. V.; Mulazzani, Q. G. On the Hydrolysis of Iodine in Alkaline Solution: A Radiation Chemical Study. *Radiat. Phys. Chem.* **2007**, *76* (6), 932–940. https://doi.org/10.1016/j.radphyschem.2006.06.009.

(27) Wren, J. C.; Paquette, J.; Sunder, S.; Ford, B. L. Iodine Chemistry in the +1 Oxidation State. II. A Raman and Uv–Visible Spectroscopic Study of the Disproportionation of Hypoiodite in Basic Solutions. *Can. J. Chem.* **1986**, *64* (12), 2284–2296. https://doi.org/10.1139/v86-375.

(28) Kelm, M.; Pashalidis, I.; Kim, J. . Spectroscopic Investigation on the Formation of Hypochlorite by Alpha Radiolysis in Concentrated NaCl Solutions. *Appl. Radiat. Isot.* **1999**, *51* (6), 637–642. https://doi.org/10.1016/S0969-8043(99)00113-X.

(29) Liu, H.; Zakhtser, A.; Naitabdi, A.; Rochet, F.; Bournel, F.; Salzemann, C.; Petit, C.; Gallet, J.-J.; Jie, W. Operando Near-Ambient Pressure X-Ray Photoelectron Spectroscopy Study of the CO Oxidation Reaction on the Oxide/Metal Model Catalyst ZnO/Pt(111). *ACS Catal.* **2019**, *9* (11), 10212–10225. https://doi.org/10.1021/acscatal.9b02883.

(30) Salmeron, M.; Schlögl, R. Ambient Pressure Photoelectron Spectroscopy: A New Tool for Surface Science and Nanotechnology. *Surface Science Reports*. April 30, 2008, pp 169–

199. https://doi.org/10.1016/j.surfrep.2008.01.001.

(31) Pérez Ramírez, L.; Boucly, A.; Saudrais, F.; Bournel, F.; Gallet, J.-J.; Maisonhaute, E.; Milosavljević, A. R.; Nicolas, C.; Rochet, F. The Fermi Level as an Energy Reference in Liquid Jet X-Ray Photoelectron Spectroscopy Studies of Aqueous Solutions. *Phys. Chem. Chem. Phys.* **2021**, *23* (30), 16224–16233. https://doi.org/10.1039/D1CP01511G.

(32) Gullikson, E. CXRO X-Ray Interactions With Matter http://henke.lbl.gov/optical_constants/ (accessed 2018 -03 -14).

(33) Stöhr, J. *NEXAFS Spectroscopy*; Springer Series in Surface Sciences; Springer Berlin Heidelberg: Berlin, Heidelberg, 1992; Vol. 25. https://doi.org/10.1007/978-3-662-02853-7.

(34) Ottosson, N.; Faubel, M.; Bradforth, S. E.; Jungwirth, P.; Winter, B. Photoelectron Spectroscopy of Liquid Water and Aqueous Solution: Electron Effective Attenuation Lengths and Emission-Angle Anisotropy. *J. Electron Spectros. Relat. Phenomena* **2010**, *177* (2–3), 60–70. https://doi.org/10.1016/j.elspec.2009.08.007.

(35) NIST X-ray Photoelectron Spectroscopy (XPS) Database, Version 3.5 https://srdata.nist.gov/xps/ (accessed 2022 -07 -05).

(36) Jolly, W. L.; Bomben, K. D.; Eyermann, C. J. Core-Electron Binding Energies for Gaseous Atoms and Molecules. *At. Data Nucl. Data Tables* **1984**, *31* (3), 433–493. https://doi.org/10.1016/0092-640X(84)90011-1.

(37) Sander, R. Compilation of Henry’s Law Constants (Version 4.0) for Water as Solvent.

Atmos. Chem. Phys. **2015**, *15* (8), 4399–4981. https://doi.org/10.5194/acp-15-4399-2015.

(38) Roose, A.; Iezzi, L.; Boucly, A.; Yang, H.; Krack, M.; Ammann, M.; Artiglia, L. Surface Propensity of Atmospheric Iodine Oxides: AIMD and LJ-XPS Investigation. https://doi.org/10.5194/egusphere-egu23-8213.

(39) Gladich, I.; Chen, S.; Vazdar, M.; Boucly, A.; Yang, H.; Ammann, M.; Artiglia, L. Surface Propensity of Aqueous Atmospheric Bromine at the Liquid-Gas Interface. *J. Phys. Chem. Lett.* **2020**, *11* (9), 3422–3429. https://doi.org/10.1021/acs.jpclett.0c00633.

(40) Ottosson, N.; Vácha, R.; Aziz, E. F.; Pokapanich, W.; Eberhardt, W.; Svensson, S.; Öhrwall, G.; Jungwirth, P.; Björneholm, O.; Winter, B. Large Variations in the Propensity of Aqueous Oxychlorine Anions for the Solution/Vapor Interface. *J. Chem. Phys.* **2009**, *131* (12), 124706. https://doi.org/10.1063/1.3236805.

(41) Egelhoff, W. F. Core-Level Binding-Energy Shifts at Surfaces and in Solids. *Surf. Sci. Rep.* **1987**, *6* (6–8), 253–415. https://doi.org/10.1016/0167-5729(87)90007-0.

(42) Truesdale, V. W.; Luther, G. W.; Greenwood, J. E. The Kinetics of Iodine Disproportionation: A System of Parallel Second-Order Reactions Sustained by a Multi-Species Pre-Equilibrium. *Phys. Chem. Chem. Phys.* **2003**, *5* (16), 3428. https://doi.org/10.1039/b303351a.

(43) Jolley, R. L.; Carpenter, J. H. Aqueous Chemistry Of Chlorine: Chemistry, Analysis, And Environmental Fate Of Reactive Oxidant Species. Oak Ridge National Laboratory and Union Carbide Corporation for the Department Of Energy, https://www.osti.gov/servlets/purl/5505533: Oak Ridge, Tennessee 37830 1982.

(44) Connick, R. E.; Chia, Y. The Hydrolysis of Chlorine and Its Variation with Temperature. *J. Am. Chem. Soc.* **1959**, *81* (6), 1280–1284. https://doi.org/10.1021/ja01515a004.

(45) Bichsel, Y. Hypoiodous Acid: Kinetics of the Buffer-Catalyzed Disproportionation. *Water Res.* **2000**, *34* (12), 3197–3203. https://doi.org/10.1016/S0043-1354(00)00077-4.

(46) Jay-Gerin, J.-P. Ultra-High Dose-Rate (FLASH) Radiotherapy: Generation of Early, Transient, Strongly Acidic Spikes in the Irradiated Tumor Environment. *Cancer/Radiothérapie* **2020**, *24* (4), 332–334. https://doi.org/10.1016/j.canrad.2019.11.004.

(47) Goulet, T.; Jay- Gerin, J. - P. On the Reactions of Hydrated Electrons with OH · and H 3 O + . Analysis of Photoionization Experiments. *J. Chem. Phys.* **1992**, *96* (7), 5076–5087. https://doi.org/10.1063/1.462751.

(48) Pimblott, S. M. Independent Pairs Modeling of the Kinetics Following the Photoionization of Liquid Water. *J. Phys. Chem.* **1991**, *95* (18), 6946–6951. https://doi.org/10.1021/j100171a040.

(49) Joseph, J. M.; Seon Choi, B.; Yakabuskie, P.; Clara Wren, J. A Combined Experimental and Model Analysis on the Effect of PH and O2(Aq) on γ-Radiolytically Produced H2 and H2O2. *Radiat. Phys. Chem.* **2008**, *77* (9), 1009–1020. https://doi.org/10.1016/j.radphyschem.2008.06.001.

(50) Trevani, L. N.; Calvo, E.; Corti, H. R. Diffusion Coefficients of Iodide in High Temperature Aqueous Solutions. *Electrochem. commun.* **2000**, *2* (5), 312–316. https://doi.org/10.1016/S1388-2481(00)00023-0.

(51) D’Angelantonio, M.; Venturi, M.; Mulazzani, Q. G. A Re-Examination of the Decay Kinetics of Pulse Radiolytically Generated Br-2 Radicals in Aqueous Solution. *Int. J. Radiat. Appl. Instrumentation. Part C. Radiat. Phys. Chem.* **1988**, *32* (3), 319–324. https://doi.org/10.1016/1359-0197(88)90028-8.

(52) Lewis, T.; Winter, B.; Stern, A. C.; Baer, M. D.; Mundy, C. J.; Tobias, D. J.; Hemminger, J. C. Does Nitric Acid Dissociate at the Aqueous Solution Surface? *J. Phys. Chem. C* **2011**, *115* (43), 21183–21190. https://doi.org/10.1021/jp205842w.

(53) Lainé, M.; Liao, Y.; Varenne, F.; Picot, P.; Michot, L. J.; Barruet, E.; Geertsen, V.; Thill, A.; Pelletier, M.; Brubach, J.-B.; Roy, P.; Le Caër, S. Tuning the Nature of the Anion in Hydrated Layered Double Hydroxides for H 2 Production under Ionizing Radiation. *ACS Appl. Nano Mater.* **2018**, *1* (9), 5246–5257. https://doi.org/10.1021/acsanm.8b01240.

(54) Church, J. A. Kinetics of the Uncatalyzed and Copper(II)-Catalyzed Decomposition of Sodium Hypochlorite. *Ind. Eng. Chem. Res.* **1994**, *33* (2), 239–245. https://doi.org/10.1021/ie00026a010.

(55) Yu, X.-Y.; Liu, B.; Yang, L. Imaging Liquids Using Microfluidic Cells. *Microfluid. Nanofluidics* **2013**, *15* (6), 725–744. https://doi.org/10.1007/s10404-013-1199-4.